



ORGANISMAL BIOLOGY

Convergence of scaffold-guided bone regeneration principles and microvascular tissue transfer surgery

David S. Sparks^{1,2,3†}, Flavia M. Savi^{1,4†}, Constantin E. Dlaska¹, Siamak Saifzadeh^{1,4,5}, Gary Brierly¹, Edward Ren¹, Amaia Cipitria^{6,7,8}, Johannes C. Reichert⁹, Marie-Luise Wille^{1,4}, Michael A. Schuetz^{1,4,10}, Nicola Ward¹¹, Michael Wagels^{2,3,12*}, Dietmar W. Hutmacher^{1,4,13*}

A preclinical evaluation using a regenerative medicine methodology comprising an additively manufactured medical-grade ϵ -polycaprolactone β -tricalcium phosphate (mPCL-TCP) scaffold with a corticoperiosteal flap was undertaken in eight sheep with a tibial critical-size segmental bone defect (9.5 cm³, M size) using the regenerative matching axial vascularization (RMAV) approach. Biomechanical, radiological, histological, and immunohistochemical analysis confirmed functional bone regeneration comparable to a clinical gold standard control (autologous bone graft) and was superior to a scaffold control group (mPCL-TCP only). Affirmative bone regeneration results from a pilot study using an XL size defect volume (19 cm³) subsequently supported clinical translation. A 27-year-old adult male underwent reconstruction of a 36-cm near-total intercalary tibial defect secondary to osteomyelitis using the RMAV approach. Robust bone regeneration led to complete independent weight bearing within 24 months. This article demonstrates the widely advocated and seldomly accomplished concept of “bench-to-bedside” research and has weighty implications for reconstructive surgery and regenerative medicine more generally.

INTRODUCTION

A combination of functional and structural reconstruction of large-volume bone loss in the load-bearing appendicular skeleton is demanding (1). Segmental large-volume bone loss in the tibia poses the biggest challenge and arises from a range of causes including infection, trauma, and malignancy. When the tibia is fractured, particularly in high-energy injuries, or instrumented to effect fixation, the already limited soft tissue envelope and its vascularity are further compromised (2). Current approaches to segmental bone defects without an overlying soft tissue deficit are multiple and include the following: limb shortening, nonvascularized autologous bone graft (ABG) alone, delayed nonvascularized autograft placed into an induced membrane (Masquelet technique) (3), distraction osteogenesis (Ilizarov technique) (4), and vascularized bone (5) with or without allograft (6). Surgical options become limited for large bone defects because of prolonged length of treatment, infectious complication's high rates of non-union, and insufficient

donor bone available to replace the volume of bone that is missing (7). Therefore, it is expected that amputation is not an infrequent outcome for such patients (8). Given these shortcomings and the increasing demand for bone regeneration in limb salvage (non-unions, bone tumors, and revision surgeries of failed arthroplasties), bone tissue engineering has received considerable scientific, economic, and clinical attention over the past two decades. Despite this, only a small portion of this work has been clinically translated (fig. S1).

Our work has focused on bench-to-bedside translation of a scaffold-guided bone regeneration (SGBR) concept that is centralized on three-dimensional (3D) printed biodegradable composite scaffolds (9). The scaffold in our study [medical-grade ϵ -polycaprolactone β -tricalcium phosphate (mPCL-TCP)] is undergoing approval by the U.S. Food and Drug Administration (FDA) and as well as CE (Conformité Européene) -marking. This composite scaffold has an extensive preclinical evidence base (10–17) involving mesenchymal stem cells, growth factors, and autologous and allogenic bone grafts in a large animal critical-sized bone defect model developed by our group (18). From this work, we concluded that critical-size bone defects should be characterized by the volume of bone that is lost, i.e., medium (M; 9.5 cm³), large (L; 14.25 cm³), and extra-large (XL; 19 cm³) (19). Furthermore, that scaffold vascularization remains a key limitation to be addressed for both L and XL bone defects. A variety of methods have been investigated to address the issue of scaffold vascularization including prevascularization before transplantation, vessel-based approaches for axial vascularization (arteriovenous loop and associated variations), and flap-based approaches for axial vascularization (muscle flaps, periosteal flaps, etc.) (20). Given the intimacy between angiogenesis and osteogenesis (21), it is reasonable to suggest that for predictable and reproducible SGBR, both processes should be synchronized (20).

Regenerative capacity of vascularized corticoperiosteal tissue is substantial (22, 23). Corticoperiosteal flaps (CPFs) have a robust

¹Centre for Biomedical Technologies, School of Mechanical, Medical, and Process Engineering, Faculty of Engineering, Queensland University of Technology, Brisbane, QLD, Australia. ²Department of Plastic and Reconstructive Surgery, Princess Alexandra Hospital, Woolloongabba, QLD, Australia. ³Southside Clinical Division, School of Medicine, University of Queensland, Woolloongabba, QLD, Australia. ⁴ARC Training Centre for Multiscale 3D Imaging, Modelling, and Manufacturing, Queensland University of Technology, Brisbane, QLD, Australia. ⁵Medical Engineering Research Facility, Queensland University of Technology, Chermside, QLD, Australia. ⁶Department of Biomaterials, Max Planck Institute of Colloids and Interfaces, Potsdam, Germany. ⁷Biodonostia Health Research Institute, San Sebastian, Spain. ⁸IKERBASQUE, Basque Foundation for Science, Bilbao, Spain. ⁹Department of Orthopaedics and Orthopaedic Surgery, University Medicine Greifswald, Ferdinand-Sauerbruch-Straße, Greifswald, Germany. ¹⁰Jamieson Trauma Institute, Royal Brisbane Hospital, Herston, QLD, Australia. ¹¹Department of Orthopaedics, Princess Alexandra Hospital, Woolloongabba, QLD, Australia. ¹²Australian Centre for Complex Integrated Surgical Solutions (ACCIS), Princess Alexandra Hospital, Woolloongabba, QLD, Australia. ¹³ARC Training Centre for Additive Biomanufacturing, Queensland University of Technology, Kelvin Grove, QLD, Australia.

*Corresponding author. Email: dietmar.hutmacher@qut.edu.au (D.W.H.); michael.wagels@health.qld.gov.au (M.W.)

†These authors contributed equally to this work.

blood supply and potential donor sites for distant transfer are plentiful (5). For fast and uniform scaffold vascularization, an axial-based intrinsic (internal) approach is considered key, and this has been successfully performed using a vessel-based method (arteriovenous loop) (24). To date, few studies have incorporated a flap-based approach for scaffold vascularization (20, 25). None have exploited the innate capacity of vascularized corticoperiosteum for SGBR and translated this clinically. We define an approach that incorporates the intrinsic axial vascularization strategy alongside a flap for matched tissue regeneration as regenerative matching axial vascularization (RMAV) (20). This study is an elegant example of the RMAV approach, where a CPF is used not only to vascularize the scaffold intrinsically but also to make available substantial numbers of mesenchymal progenitor cells within the scaffold architecture and thereby stimulate bone regeneration (Fig. 1A).

We describe a preclinical animal study using an M critical-sized bone defect model to establish the efficacy of the RMAV approach compared with a scaffold control (mPCL-TCP only) and a clinical gold-standard control (ABG; Fig. 1B). We then describe the results of this integrative technique for an XL critical-sized bone defect in a pilot study of two sheep. We also describe translation of this concept in a 27-year-old patient with subtotal segmental loss (36-cm intercalary defect) of the tibia. The current study represents the rare bench-to-bedside translation of a tissue engineering technique to

reconstruct major bone loss in the load-bearing limb where contemporary surgical options are limited, taking the marriage between SGBR and modern surgical practice to new heights.

RESULTS

In vivo study

Sheep model characteristics

Surgery was performed as described in detail elsewhere (18). Briefly, of the tibial mid-diaphysis, 3-cm (M size, 9.5 cm³) and 6-cm (XL size, 19 cm³) segmental defects were created and subsequently stabilized using a 10-hole or 12-hole dynamic compression plate (DCP; Synthes). At the time of surgery, weight ranged from 45 to 50 kg and all sheep were of mature age (6 to 8 years old) to ensure that secondary remodeling of skeletal bone had occurred.

Three groups were evaluated as part of the primary preclinical study involving the M size defect. These included defects treated with (i) mPCL-TCP scaffold alone, (ii) mPCL-TCP scaffold and CPF, and (iii) ABG alone (Fig. 1B and table S1). An additional proof-of-principle study was performed using an increased XL defect size, treated with mPCL-TCP scaffold and a CPF. In this latter pilot study, one sheep was evaluated for a total study time length of 15 months and the other for 12 months. Results of the mPCL-TCP scaffold alone and ABG groups for the M size defect

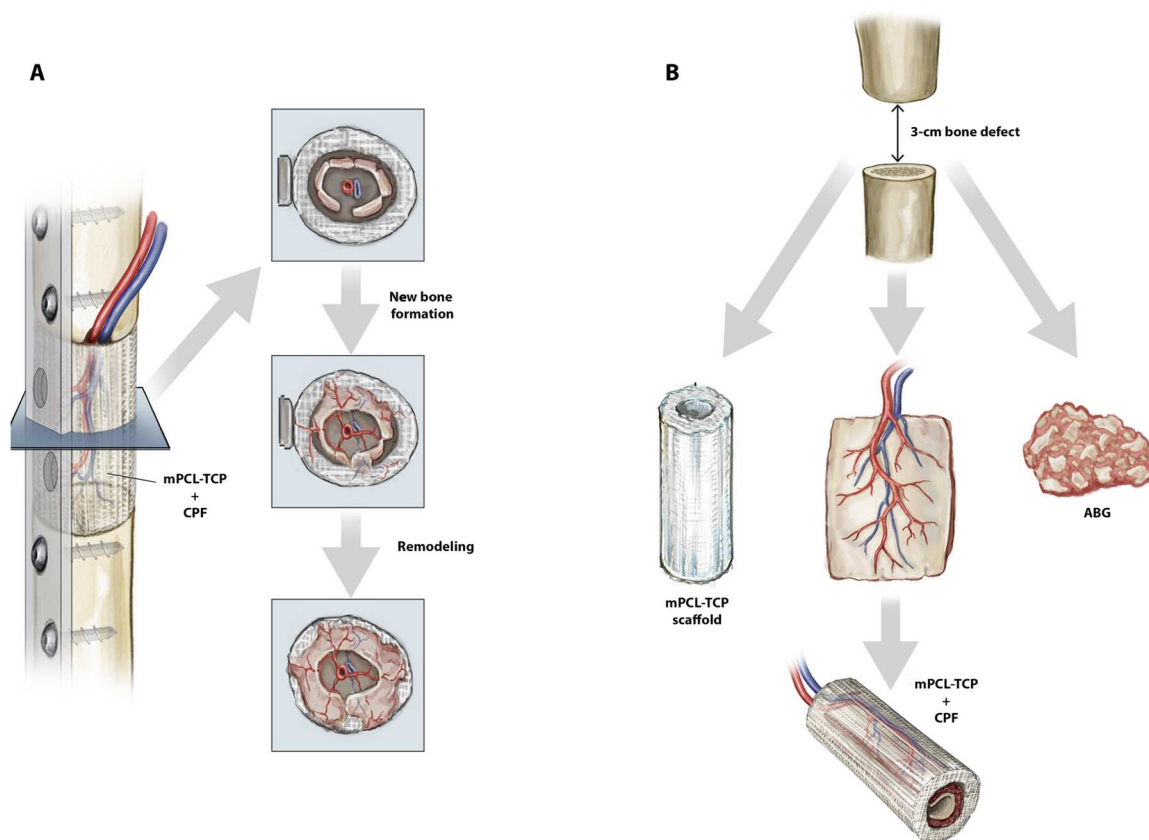


Fig. 1. Schematic illustrating the M size defect study and the RMAV concept for bone regeneration. (A) The process of bone healing induced through the RMAV concept is illustrated. (B) Different treatment groups in the M size (3 cm in length) segmental bone defect in vivo study. The different groups for reconstruction of the segmental bone defect in the study included mPCL-TCP scaffold only, a CPF placed internally within the mPCL-TCP scaffold for RMAV and bone autograft from the iliac crest as a gold standard comparator. Credit: Beth Croce.

study were obtained from previous work by the research group (17). All animals survived the study period of 12 months and were healthy throughout. There were no infections, osteosynthesis failure, or signs of foreign body reaction in those sheep where scaffold implants were used.

X-ray analysis for M size defect

For the animals, internal fixation and proximal/distal segment alignment were confirmed immediately postoperatively. Throughout the 12-month radiographic assessment period, there was no screw loosening, implant disruption, or valgus deformity of the tibia observed. At 3 months, bone defect bridging was observed in all eight sheep treated with ABG (100%; Fig. 2, A to H), in seven of eight sheep treated with mPCL-TCP + CPF (88%; Fig. 2, P to X), and in three of seven for the mPCL-TCP group (42%; Fig. 2, I to O). Radiographic bone healing showed a clear trajectory toward increased bone formation and remodeling throughout the study period for mPCL-TCP + CPF and ABG groups [Fig. 2 (I to O) and Fig. 2 (A to H), respectively]. By 12 months, bone formation occupied 75 to 100% of the defect for these same groups and appeared more uniform in distribution in most animals compared to the mPCL-TCP group. In contrast to ABG where signs of remodeling were evident in most sheep at 12 months, remodeling was delayed in mPCL-TCP + CPF (gross signs present in only two sheep; Fig. 2, P to X). Remodeling was not observed in the mPCL-TCP group because of a lack of gross bone formation (Fig. 2, I to O). Interval radiographic assessment for the mPCL-TCP + CPF group can be found in the Supplementary Materials (fig. S2), with results for mPCL-TCP alone and ABG groups found in the original work by our group (17).

Biomechanical strength for M size defect

Values for torsional stiffness were comparable for mPCL-TCP + CPF and ABG groups ($P = 0.46$; Fig. 3A), with both having a significantly higher torsional stiffness compared to the mPCL-TCP group ($P < 0.001$ and $P < 0.0001$, respectively). In addition to this, the mPCL-TCP + CPF group had a significantly stronger torsional moment compared with the mPCL-TCP group ($P < 0.001$; Fig. 3B), although this was less than the ABG group ($P < 0.001$; Fig. 3B).

Bone volume regenerate for M size defect

Total bone volume regeneration was highest in the mPCL-TCP + CPF and ABG groups and was significantly different to the mPCL-TCP group ($P < 0.0002$; Fig. 3C). Bone volume distribution appeared to be predominantly in the proximal and distal sites of the defect for all groups (Fig. 3D). For the mPCL-TCP + CPF group, bone volume regenerate seemed to occur more predominantly in the proximal component of the defect, although significant new bone was also observed distally, which are results that were comparable to the ABG group (Fig. 3D). A significant increase in bone volume regenerate was observed between the middle portions of the mPCL-TCP + CPF group compared with the mPCL-TCP group ($P < 0.003$; not shown in figure). For axial distributive bone volume (endosteal, scaffold wall, and periosteal; Fig. 3E), the mPCL-TCP + CPF group had more bone regenerate within the scaffold wall than within the endosteal ($P = 0.0002$) or periosteal areas ($P = 0.0002$) and substantially more than the scaffold wall of the mPCL-TCP group ($P < 0.0007$).

Histological analysis and scanning electron microscopy results for M size defect

Bone formation was seen in all specimens. For the M size defect mPCL-TCP group, at 12 months, bone formation was mainly observed proximally, around the scaffold struts along the fixation plate (fig. S3). The M size defect ABG group had more uniform bone growth throughout the defect, achieving notable remodeling at 12-month time point (fig. S3). The M size critical-sized defect mPCL-TCP + CPF group showed large amounts of bone formation centrally and through the scaffold at 12 months after surgery (Figs. 4, B to D, and 5A, and fig. S4, C, D, and K). Further histological analysis of this group using Goldner's trichrome revealed good integration of host bone with newly formed bone tissue emanating from the CPF (Fig. 4, E to G, and fig. S4, E to G).

Scanning electron microscopy (SEM) and Picrosirius red (PSR) polarized light images depicted an active healing response. At the distal interface (Fig. 4H), osseointegration of the host bone (green) with Haversian canals (red) advancing through the interface of the newly formed bone tissue (Fig. 4I, white arrows and arrowheads, respectively) could be observed. At the periphery of the mPCL-TCP-coated scaffold wall, intussusceptive angiogenesis

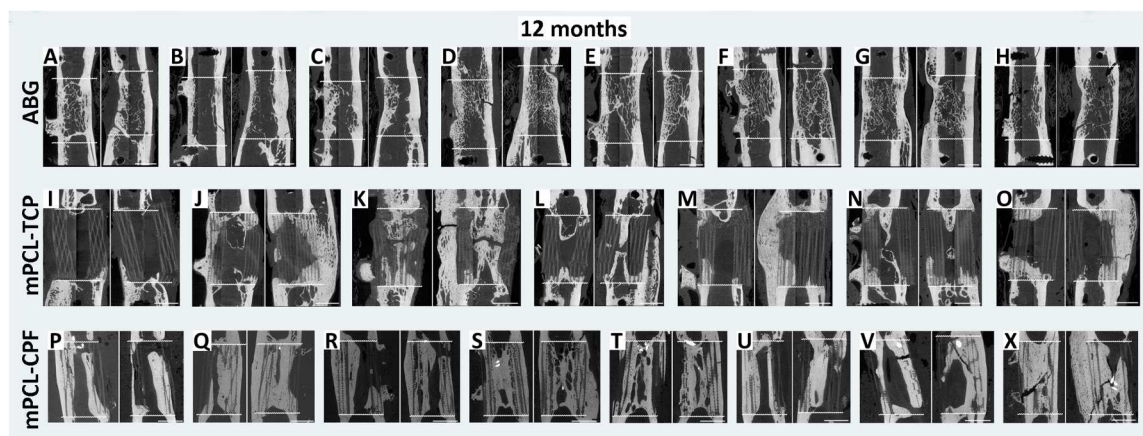


Fig. 2. Representative 2D μ CT at 12month images of an M size defect for all treatment groups. - M size defect group treated with ABG (A to H) ($n = 8$), the MN size defect group treated with mPCL-TCP scaffold only (I to O) ($n = 7$), and the M size defect group treated with mPCL-TCP scaffold combined with CPF (P to X) ($n = 8$). Dotted lines are delimitating the defect size. Scale bars, 1 cm

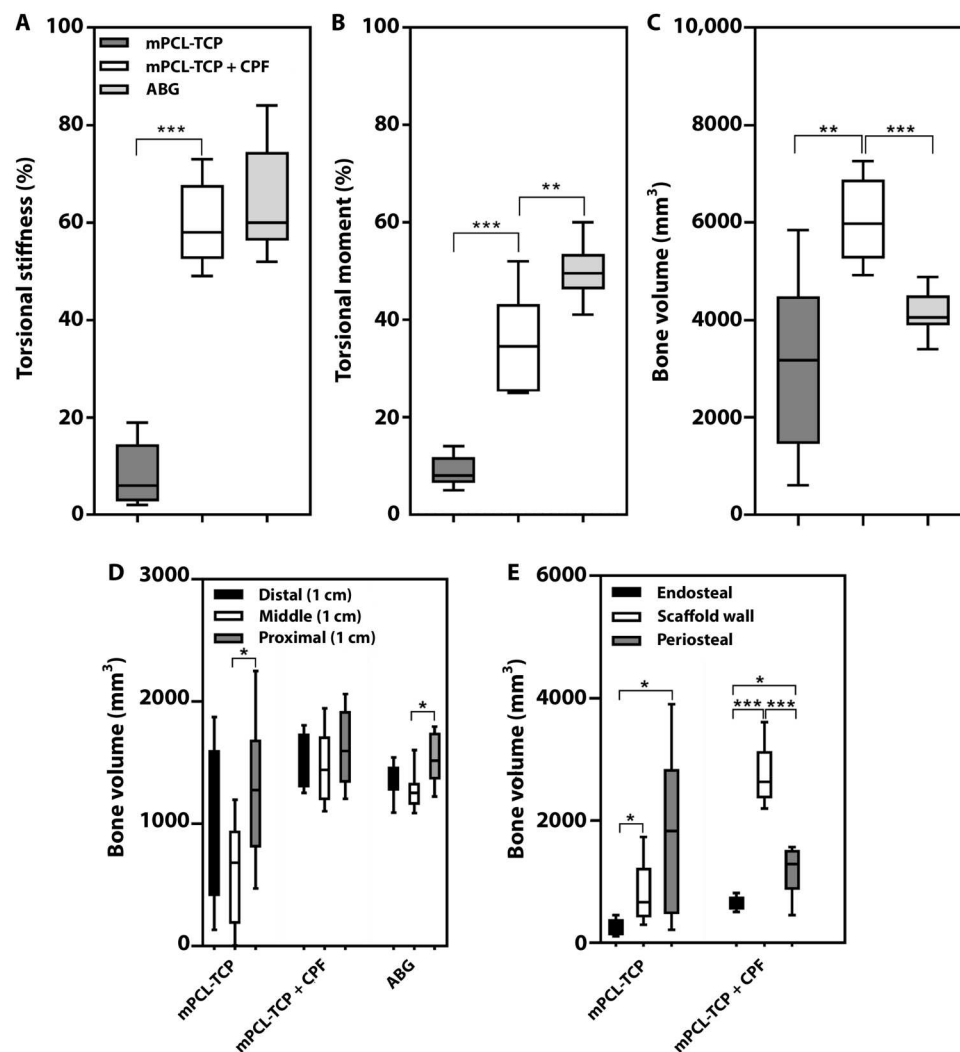


Fig. 3. Results of biomechanics and μ CT for all three groups in the M size defect study. Torsional stiffness (A) and torsional moment (B) graph comparing mPCL-TCP, mPCL-TCP + CPF, and ABG groups. Total bone volume comparing mPCL-TCP, mPCL-TCP + CPF, and ABG groups (C). Longitudinal bone volume regenerate distribution in the proximal, middle, and distal sites of the defect for the mPCL-TCP, mPCL-TCP + CPF, and ABG groups (D). Axial bone volume regenerate distribution within the endosteal, scaffold wall, and periosteal sites of the defect for the mPCL-TCP and mPCL-TCP + CPF groups (E). * $P < 0.05$, ** $P < 0.01$, and *** $P < 0.001$.

forming two parallel capillaries (Fig. 4H, black arrows) from the CPF axial vasculature was also seen.

Initial bone apposition was observed directly around the mPCL-TCP-coated wall (Fig. 4J, red arrowheads), with a highly ordered canalicular network (Fig. 4K) running along the concentric lamellae and perpendicular to the collagen fibers (Fig. 4L, white arrowheads). On closer inspection, osteocytes (Fig. 4K, green) were in direct contact with the mPCL-TCP scaffold (Fig. 4K, blue), with its canaliculi extending toward the surface of the TCP-coated wall (Fig. 4K, red arrow) and bone laid down outward from the implant surface. In addition, the presence of the cement line (Fig. 4K, black arrow) and the positioning of the perilacunar tissue around the mPCL-TCP wall indicating de novo bone formation was also seen. This was oriented to withstand loading transfer from the mPCL-TCP interface and surrounding tissue. These results were further confirmed by the polarized light microscopy around the

mPCL-TCP scaffold struts showing the presence of collagen fibers aligned along the osteocytes long axis (Fig. 4L).

Differentiating osteogenic cells (osteoblast-osteocyte like, Fig. 4M, red arrowheads) could be seen at the vicinities of the CPF remnants (Fig. 4M, green porous tissue with spindle-shaped osteocytes with reduced volume). Although the CPF was well incorporated into the scaffold wall (Fig. 3E), there was a large presence of immature collagen fibers within the scaffold wall region as shown by polarized light (Fig. 4L, green fibers) and at the new lamellar bone formed at the middle region of the defect site (Fig. 4N, white arrows). In areas of localized remodeling (Fig. 4J, green color), several osteoblast-osteocyte-like and collagen fibers that were poorly ordered (Fig. 4J, black head arrows at the green region) were found. These localized areas with high proportion of osteoblast-osteocytes and immature structure were further confirmed by immunohistochemical staining of collagen type I (Fig. 5B) and type II (Fig. 5C), showing stronger reactivity at localized areas of

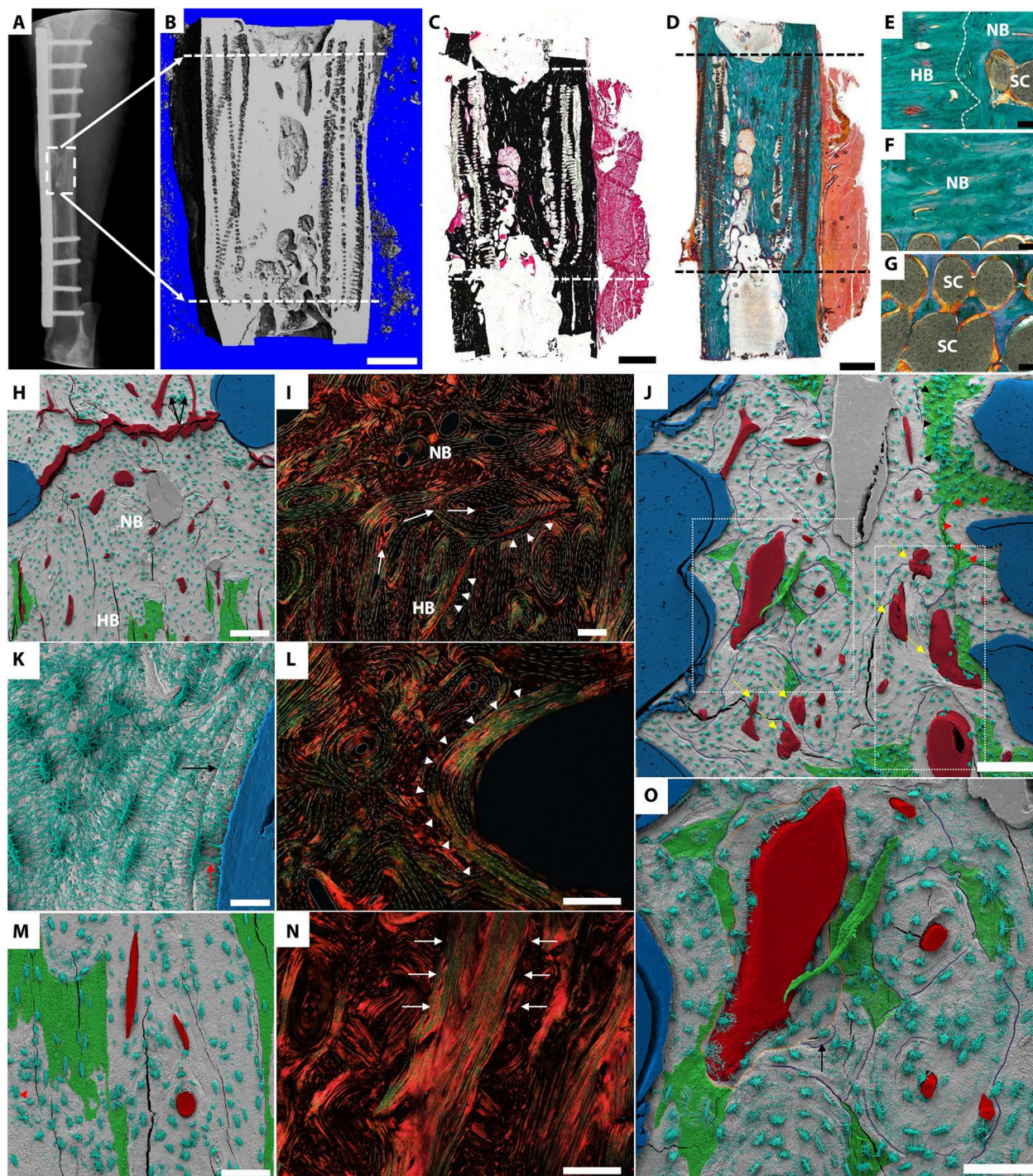


Fig. 4. Cumulative radiological, histological, SEM, and light polarized results for a representative M size mPCL-TCP + CPF sheep at 12-month sacrifice. (A) Plain x-ray and (B) μ CT imaging reveals bony union alongside features of bone remodeling with trabecular formation throughout the internal defect component. Undecalcified resin section stained with (C) von Kossa and (D) Goldner's trichrome (GT) showing good integration of the host bone and newly formed bone tissue. (E) Higher magnification of GT showing the interface between host bone (HB) and the new bone (NB) formed. (F and G) Higher magnification of GT showing the osteointegration of new bone formed and scaffold (SC). (H and I) SEM and LP images showing the ultrastructural morphology of newly formed bone and its interaction with host bone. (J) Osteocyte network and neovascularization (red, blood vessels) within scaffold interstruts and areas of localized bone remodeling (green, woven bone). (K and L) Ultrastructural morphology of the new tissue formed (white arrowheads) around the scaffold strut (blue) and an osteocyte (red arrow) in direct contact with the mPCL-TCP scaffold. (N) lamellar bone. (M) Host tissue interface (green) with new bone, showing the porous characteristic of host tissue with spindle shaped osteocytes and reduced body volume. (O) Osteocyte's arrangement around long blood vessels, which appears to be etched deeper (orange line) than the adjacent tissue, indicating mineral compositional differences; osteocyte encasement within osteoid (black arrow). Dashed line, defect site. Scale bars, (B to D) 5 mm, (E to H and J) 200 μ m, (I and L to O) 100 μ m, and (K) 20 μ m.

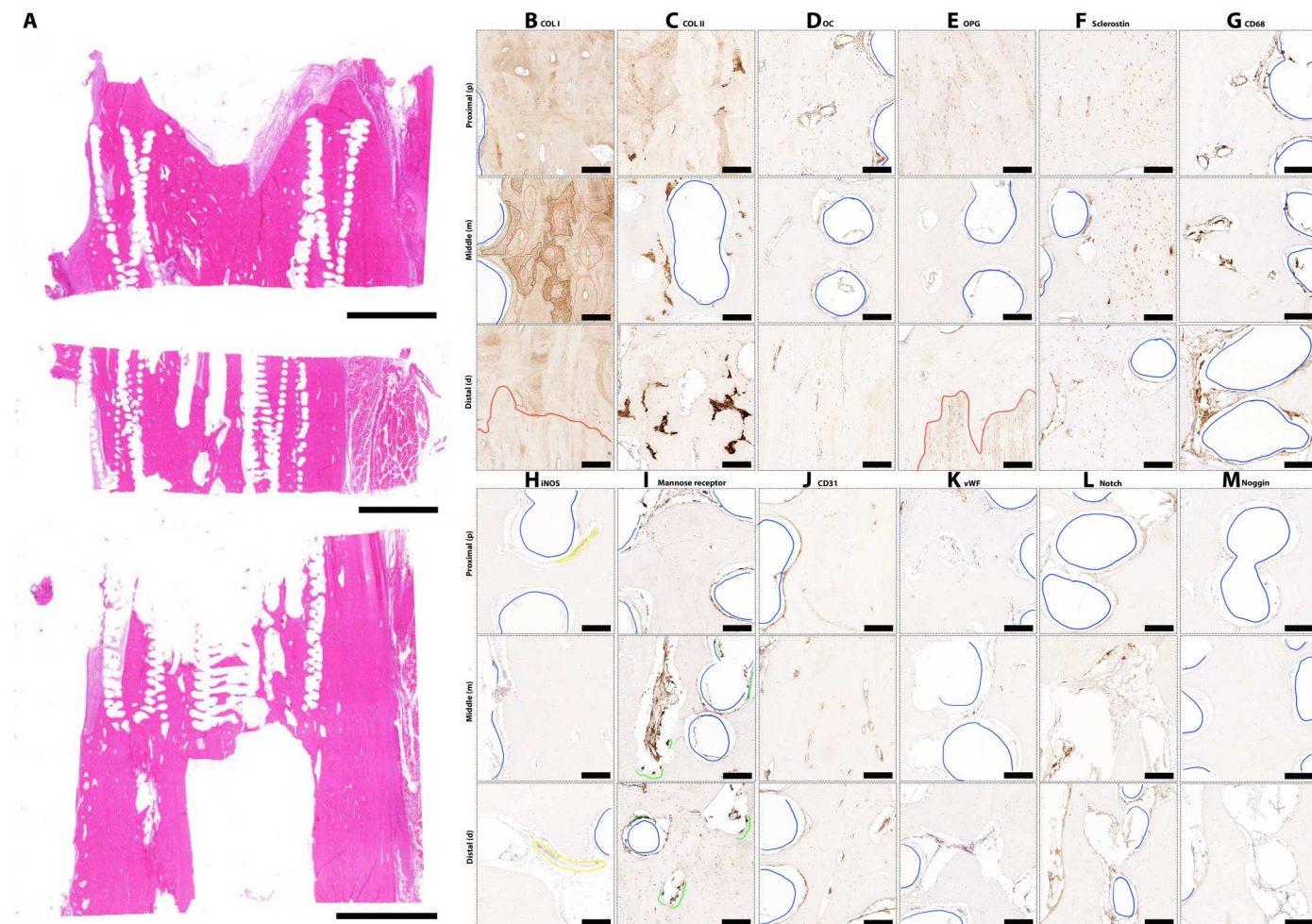


Fig. 5. Cumulative immunohistochemistry results for a representative M size mPCL-TCP + CPF sheep at 12-month sacrifice. (A) Sections of hematoxylin and eosin (H&E) were proximal (p), middle (m), or distal (d) when analyzed with IHC. Staining was as follows: (B) collagen type 1 (COL I), (C) collagen type II (COL II), (D) OC, (E) OPG, (F) Sclerostin, (G) CD68, (H) iNOS, (I) mannose receptor, (J) CD31, (K) vWF, (L) Notch, and (M) Noggin. Isotypes, fig. S10. Blue lines, scaffold; red lines: host and new bone interface; yellow lines, blood vessels; green line, macrophages. Scale bars, (A) 5000 μm and (B to M): 200 μm .

woven bone (Fig. 5B, black lines) next to areas of lamellar bone (Fig. 5B, red lines), as well as remnants of cartilage containing osteocytes in lacunae (Fig. 5C). In areas adjacent to the mPCL-TCP-coated scaffold wall, osteocytes were arranged around long blood vessels, which appeared to be etched deeper than the adjacent lamellae with clear mineral compositional differences between the two areas (Fig. 4O, orange line). On closer evaluation, osteoid-osteocyte (osteoblasts within osteoid) appeared to have a smaller number of canaliculi, and an osteoid-osteocyte was encased in the bone matrix (Fig. 4O, black arrow).

Large vessels sprouting along the CPF axial vasculature were seen throughout the defect, and immediate vascular supply at the vicinity of the mPCL-TCP was also seen (Fig. 4J, yellow arrows). Furthermore, an extensive osteocytic network was observed throughout the newly formed bone. Secondary osteon bone formation was present at the interface of the mPCL-TCP scaffold struts and CPF remnant with osteocytes in direct contact with the blood supply (Fig. 4O). Further SEM results for all animals of the mPCL-TCP + CPF group can be found in the Supplementary Materials (fig. S5).

Immunohistochemistry analysis for M size defect

Large volumes of collagen type I deposition was broadly found within the newly formed bone, at the proximal (Fig. 5B, p), middle (Fig. 5B, m), and distal sites of the defect (Fig. 5B, d) and invaginating the mPCL-TCP scaffolds. The synthesis of collagen type I appeared to have greater immunohistochemical reactivity at localized areas of bone remodeling [Fig. 5B (m), black lines]. These areas displayed high proportion of osteoblast-osteocytes surrounded by randomly oriented collagen fibers [Fig. 5B (m), black lines] next to areas of lamellar bone with collagen fibers arranged in longitudinal fashion [Fig. 5B (m), red lines]. Positive collagen type II reactivity was seen at areas of calcified cartilage next to these woven bone regions and at the vicinities of the mPCL-TCP-coated scaffold wall (Fig. 5C, p to d), indicating extracellular matrix shift from woven bone to lamellar via chondro-osseous accumulations.

Osteocalcin (OC) expression was detected at osteocytes at the proximal (Fig. 5D, p) and distal (Fig. 5D, d) sites of the defect and at the osteoblasts lining the extracellular and cytoplasmic content of the newly formed bone and herein was also found along the mPCL-TCP scaffold walls (Fig. 5D, m). Osteoprotegerin

(OPG) is an osteoclast inhibiting factor and growth factor secreted by the extracellular matrix in ABG, which is a key regulator in osteoclast differentiation and activation (26). OPG is therefore essential for bone resorption and was highly expressed at the proximal and distal sites at the defect, specifically in the host bone [Fig. 5D (p and d), red lines]. Sclerostin as one of the first mediators between osteocytes, osteoblasts, and osteoclasts talk is critical for bone remodeling, especially by antagonizing bone and cartilage formation. High sclerostin expression was observed at the middle site (Fig. 5F, m) of the defect at areas of lamellar bone deposition within osteoblasts potentially reaching the osteocytic stage, at osteocytes within the proximal and distal sites of the defect (Fig. 5F, p and d), as well as at small islands of mineralized cartilage. Sclerostin signal was also observed at the extracellular and cytoplasmic content of future Haversian canals of the newly regenerating bone and at the mPCL-TCP-coated scaffold walls (Fig. 5F, m).

Staining for CD68 was strong in all specimens, especially at resorption sites and around the mPCL-TCP-coated scaffold struts demonstrating osteoclastic and phagocytic activity (Fig. 5G, p to d). These results were further confirmed by local infiltrate of M1 [inducible nitric oxide synthase (iNOS)] around the mPCL-TCP-coated scaffold wall and within the endothelial content of future Haversian canals and blood vessels [Fig. 5H (p to d), blue line and yellow line, respectively] and M2 (mannose receptor) macrophages, especially at osteoclasts at resorption areas and at the vicinity of the mPCL-TCP-coated wall [Fig. 5I (p to d), green lines]. These results further demonstrate the macrophage importance in the suppression of inflammation, in the synthesis of vascular growth, and also contribution to tissue repair and remodeling.

Blood vessels mediating angiogenesis express high levels of CD31 (platelet endothelial cell adhesion molecule 1). These types of capillaries (defined as type H) (26) are intermittently present at corticoperiosteal regions of long bones. Endothelial cells lining newly forming blood vessels within the regenerating bone were heavily stained with CD31, especially within the central regions and around the mPCL-TCP scaffold architecture (Fig. 5J, p to d). Similarly, von Willebrand factor (vWF) staining, was seen at the basement membrane of new blood vessels within forming osteons and within the central regions and wall of the mPCL-TCP scaffold architecture throughout the defect site (Fig. 5K, p to d). *Notch*, derived from endothelial precursors, is a key mediator involved in bone remodeling, osteoclast activation, and differentiation of osteoblasts into functional osteocytes (27). *Notch* activity was present at the endothelial wall of blood vessels surrounding the mPCL-TCP struts, as well as within the endothelial wall of blood vessels at bone resorption sites (Fig. 5L, p to d). However, *noggin* activity was found to be neglected (Fig. 5M, p to d).

Proof-of-principle study results for XL size defect

Bone non-unions can be temporally, clinically, and radiologically diagnosed. Yet, ill-defined, non-union can be regarded as the complete failure of the bone regenerative capabilities. The FDA has established fracture non-union as the arrest of bone healing within a period of 9 months after injury, followed by the absence of progressive signs of bone repairing within the successive next 3 months (28). However, variations of these temporal parameters have been described (29). Therefore, after consultation with orthopedic and plastic/reconstructive surgeons, we performed a proof-of-principle study doubling the segmental defect size with the aim to reproduce a non-union.

Two sheep received an XL size mid-diaphyseal segmental bone defect of the tibia using the established surgical approach (18), stabilized with a 12-hole DCP (Depuy, Synthes). These sheep were both treated with an mPCL-TCP-coated scaffold combined with a CPF. Uniform bone formation was found throughout the defect with bridging of the defect site observed as early as 3 months and complete union achieved after 12 months for both sheep (Fig. 6A and fig. S6A). Bone volume regenerate was robust throughout the scaffold, further confirmed by micro-computed tomography (μ CT) analysis (Fig. 6B and fig. S6B). Histological evaluation using Safranin O/von Kossa (fig. S6C) and Goldner's trichrome (fig. S6, D to G) revealed substantial mineralized formation both throughout the scaffold and at the proximal and distal interfaces with the newly formed bone. High magnification images of the Goldner's trichrome staining revealed good integration of the host tissue with the new tissue formed, as well as bone formation around the mPCL-TCP scaffold struts (fig. S6, E to G). SEM analysis reflected an active healing process with clear distinguishable secondary osteon formation and the presence of osteocytes and blood vessel supply (fig. S6, H to J). The new bone tissue formed stained positive for collagen type I [fig. S6, L (p) to P (d)], where unorganized cancellous/trabecular bone could be observed, especially at the middle site of the defect (fig. S6L, m). Some extent of mineralized cartilage was detected by collagen type II staining within the proximal, middle, and distal sites of the defect (fig. S6M, p to d). OC expression was detected in osteocytes and at resorption regions of the defect site (fig. S6N, p to d). For the 15-month time point (XL size defect; Fig. 6), the expression of the collagen I [Fig. 6, L (p) to P (d)] and OC (Fig. 6N, p to d) were lesser than the 12-month sample; however, the collagen type II expression was higher (Fig. 6M, p to d). OPG and sclerostin expression were similar for the 12- and 15-month time point, as well as for the M size volume defect (fig. S6, O and P; Figs. 6, O and P, and 5, E and F, respectively). Macrophagic activity, depicted by CD68 staining, was mainly observed at the outer surface of the mPCL-TCP scaffold struts and at resorption areas where osteoclastic activity was occurring (fig. S6Q and Fig. 6Q). M1 (fig. S6R and Fig. 6R) and M2 (fig. S6S and Fig. 6S) macrophage activities were mainly observed around the mPCL-TCP-coated scaffold. The new tissue formed was well vascularized, showing CD31- and vWF-positive reaction at the vascular endothelial tissue within resorption sites and within the Haversian canals of the bone tissue (fig. S6, T and U, and Fig. 6, T and U). Strong expression of *Noggin* was observed also within the vascular tissue within resorption sites (fig. S6W and Fig. 6W), and *Notch* activity was negligible (fig. S6V and Fig. 6V).

Case report

On the 6 August 2017, the patient underwent reconstruction of a 36-cm intercalary defect of the tibia secondary to osteomyelitis. This was performed with definitive bony stabilization, insertion of a 3D-printed scaffold augmented with CPFs, rhBMP-7 (recombinant human bone morphogenetic protein-7; Stryker Biotech, Hopkinton, USA), and soft tissue coverage (Fig. 7, A to F). The scaffold was designed on the basis of CT images conducted on both lower limbs and manufactured using the same mPCL-TCP scaffold used in the preclinical study (see Materials and Methods). The technical aspects of this procedure were informed by the work

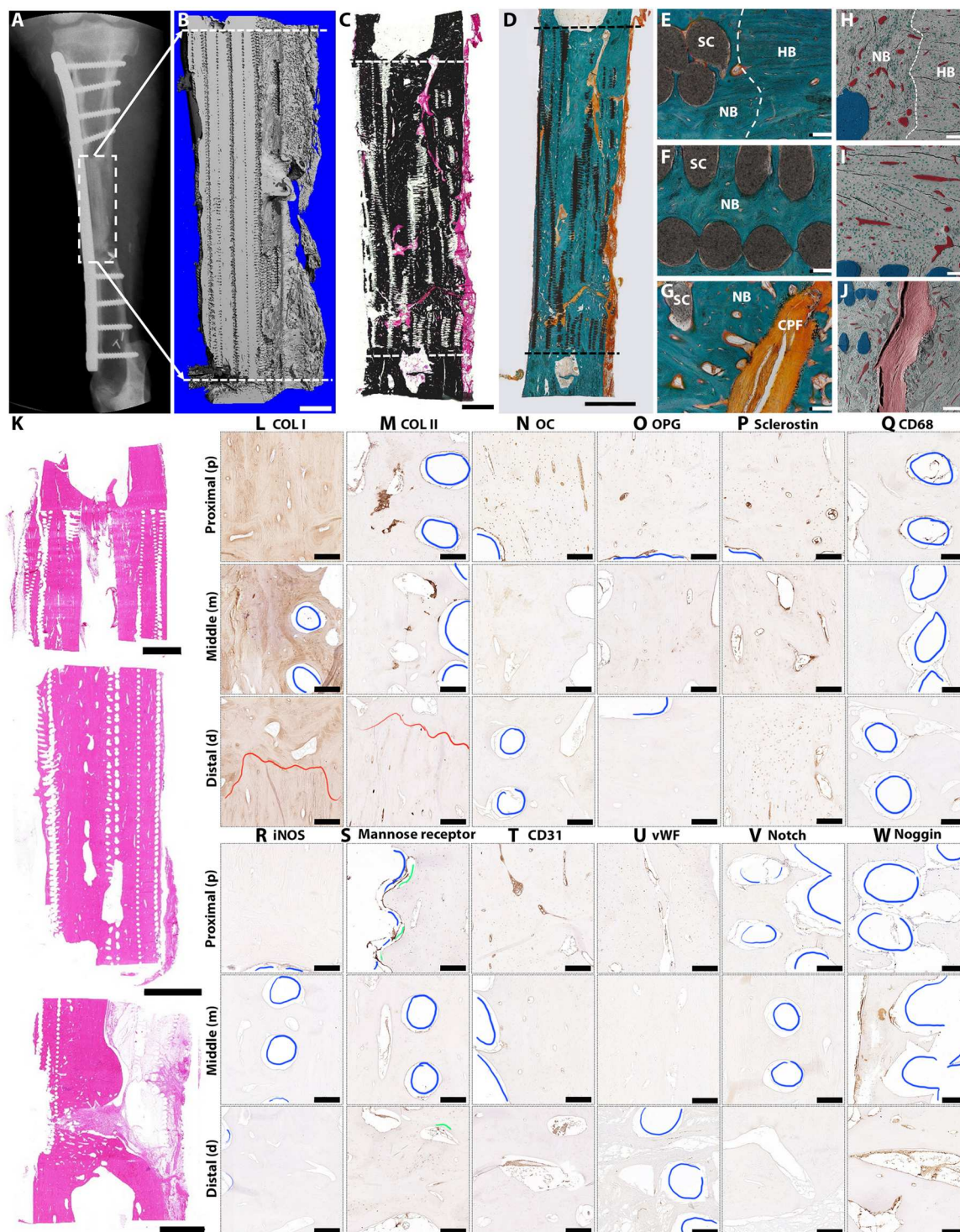


Fig. 6. Representative overview of the XL size tibial CPF pilot study results. (A) X-ray image at 15 months' time point. (B) Sagittal plane of the µCT 3D reconstruction. (C) Von Kossa-stained resin section showing good integration of the host bone and newly formed bone tissue. (D to G) Undecalcified resin section stained with Goldner's trichrome showing excellent osteointegration of host bone, scaffold, and newly formed bone. (H) SEM images showing the osteocyte network of the newly formed tissue with newly formed bone in the middle of the defect site (I) and clear neovascularization marginating alongside new bone formation (J). (K) Sections of H&E were proximal (p), middle (m), or distal (d) when analyzed with IHC. Staining was as follows: (L) collagen type 1 (COL I), (M) collagen type II (COL II), (N) OC, (O) OPG, (P) Sclerostin, (Q) CD68, (R) iNOS, (S) mannose receptor, (T) CD31, (U) vWF, (V) Notch, and (W) Noggin. Scale bars, 200 µm. Dashed line, defect site. Scaffold collapse in (C) resulting from sample processing. Blue lines, scaffold; red lines, host and new bone interface; green line, macrophages. Isotypes, fig. S11. Scale bars, (B, C, and K) 5 mm, (D) 10 mm, (E to I and L to W) 200 µm, and (J) 500 µm

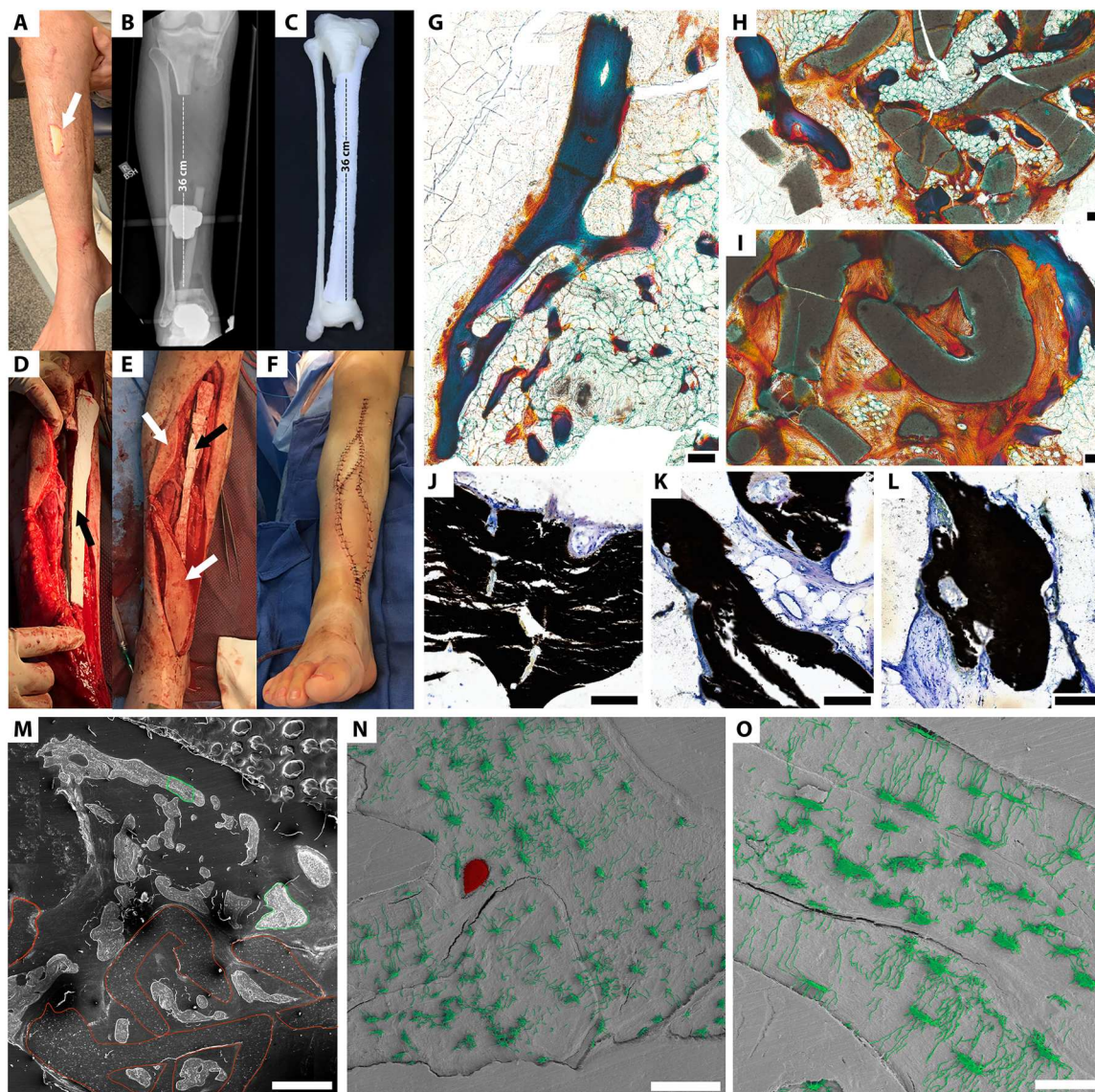


Fig. 7. Representative overview of the clinical case including intraoperative imagery, histological and scanning electron microscopy results. (A) The patient's limb at presentation with the area of exposed tibia indicating clinical osteomyelitis (white arrow), which, following resection, left a 36-cm segmental defect of the tibia (B). The defect was 3D modeled from reconstructed CT imaging to create the mPCL-TCP scaffold construct (C) for formal reconstruction. After intramedullary nail fixation, the posterior scaffold was inset to the defect before placement of the cutaneous-CPF and the cutaneous-corticoperiosteal medial femoral condyle flap (black arrow). Following this, the anterior scaffold was inset to the defect (D) (black arrow), and the skin was closed (E and F) using the skin paddles from the flaps for additional soft tissue coverage and flap monitoring (white arrows). (I) One-year time point biopsy. During the change of internal nail fixation at 1-year time point, a core biopsy was taken, which confirmed functional bone healing. (G to I) Undecalcified resin section stained with Goldner's trichrome. (J to L) Undecalcified resin section stained with von Kossa McNeal's trichrome. (M) SEM image showing the osteocyte network of the newly formed tissue (red line scaffold). (N) An island [bottom green line image (M)] of osteocytes in the vicinity of a scaffold strut. (O) Higher magnification of the osteocyte network. Scale bars, (G to L) 200 μ m, (M) 1 mm, (N) 100 μ m, and (O) 50 μ m.

done in the animal studies. Briefly, this involved retrograde intramedullary nail fixation of the tibia followed by insertion of the scaffold in two halves (anterior and posterior components). An ipsilateral fibula CPF was placed inside the proximal scaffold with its pedicle in continuity with a medial femoral condyle CPF, which was anastomosed in a "flow-through" configuration with the distal peroneal vessels and placed in the distal scaffold. BMP-7 was impregnated into the scaffold alongside fibrin glue. As part of the flap reconstruction, two skin paddles (one from each flap) were

used for soft tissue coverage of the leg and to facilitate postoperative monitoring. There were no intraoperative or postoperative complications; both skin paddles were viable throughout the postoperative course and, as a surrogate, were considered to validate buried corticoperiosteal tissue viability. A schematic of the operative sequence can be found in the Supplementary Materials (fig. S7).

The patient's weight-bearing status was gradually increased commensurate with bone regeneration. An exchange of the intramedullary nail was performed at 12 months postoperatively, and a

small unicortical non-union involving part of the distal scaffold-bone regenerate was debrided and grafted with iliac crest ABG at 18 months. The debrided specimen was analyzed using Goldner's trichrome, von Kossa MacNeil's stains, and SEM (Fig. 7, G to O). New bone and soft tissue formation were observed within the mPCL-TCP scaffold struts remnants (Fig. 7, G to L). The SEM analysis revealed a viable network of osteocytes, as well as the presence of new blood vessel formation (fig. 7M - O). Following this procedure, the patient commenced partial weight bearing and had achieved full weight bearing at 24 months postoperatively. The residual restriction in range of motion at the knee and ankle joints has resulted in a gait that is antalgic but functional (movie S1). The patient has been reviewed at clinically appropriate intervals now for the past 4 years without complication (movie S2).

DISCUSSION

Today, therapeutic approaches for the reconstruction of large bone volume defects have outcomes that are inconsistent. Surgical approaches are many, and there is no clear indication for the use of one over another for a given set of circumstances. As a result, research has focused on the development and translation of patient-specific therapeutic concepts for bone regeneration. Tissue engineering is a research frontier in this regard. However, bench-to-bedside translations are rare (fig. S1). In this study, we show that the combination of a 3D printed biodegradable scaffold in combination with a CPF can regenerate M size critical bone defects in a long-term large animal model with near equivalence to the clinical gold-standard ABG and can be safely extended to an XL size bone defect to produce robust bone healing. Furthermore, we successfully translate the RMAV approach to reconstruct the largest long bone defect reconstructed using a 3D printed scaffold to date.

Vascularization precedes the creation of new bone and cartilage during development and is key to ongoing bone viability and remodeling capacity (30). In neo-osteogenesis, vascularization ensures sufficient delivery of osteoclast precursors and osteoprogenitor cells to the site of osseous induction (31), and certainly, the existence of direct molecular interactions between endothelial and osteoblastic cell lineages provides further credence to the concept of coupling between new blood vessel formation and osteogenesis (27). Hence, the osseous induction in SGBR is based on sufficient and uniform neovascularization, with cell function severely limited by a diffusion distance greater than 200 μ m from a blood vessel (32). Most previous approaches to axially vascularize scaffolds for tissue regeneration, use an "extrinsic" approach whereby the scaffold is vascularized externally from surrounding vascular tissue (20). The internal aspect of the scaffold, particularly for a large construct (as for XL defects), is vulnerable to insufficient vascularization and thus limits regenerative potential. Clinical use of the extrinsic approach has been implemented by Warnke *et al.* (33) with the use of the latissimus dorsi muscle for prelamination of a scaffold in the reconstruction of a mandibular critical-sized bone defect in 2004. An alternative to the extrinsic vascularization approach is the use of an arteriovenous axis to provide an "intrinsic" blood supply to the construct. The intrinsic approach is not new. Erol and Spira (34) developed the arteriovenous loop model in 1980, and this concept was further expanded upon by Cassell and co-workers (35). Most recently, Horch and co-workers (36) used the arteriovenous loop technique alongside a 3D printed scaffold for the

reconstruction of a critical-size tibial defect secondary to osteomyelitis as in our case (36).

What makes our concept unique is what we term RMAV (20), where the integration of an ideal axially vascularized autologous tissue source is "matched" to the intended tissue type for regeneration. This process is combined with a scaffold, which serves, in this case, as an osseoconductive conduit to accelerate and guide the tissue regenerative process. In essence, vascularized precursor tissues of the required tissue type(s) for reconstruction are incorporated into the approach for axial vascularization of the scaffold. This is in the form of a flap and makes use of a patient's tissue regenerative capacity by directing autologous growth factors and regenerative cells already endogenous to the host tissue into the scaffold, while providing an arterial supply and venous drainage. The regenerative capacity of the periosteum is well known (22), and the harvest of a thin layer of cortical bone alongside the periosteum helps preserve the inner cambium layer (22), known to be a high-density source of precursor cells for new bone formation (37). The mPCL-TCP scaffold (fig. S8) is known to support attachment, migration, and proliferation of bone precursor cells (15). In combination with corticoperiosteal tissue transfer, we were able to demonstrate robust bone regeneration in preclinical 3-cm (M size) and 6-cm (XL size) segmental bone defect models.

Our results support the bone regenerative process in a stepwise manner (Figs. 1B and 4 to 6 and figs. S2 to S6) with angiogenesis, stimulation of osteoprogenitor cells, and new woven bone formation from the CPF internally through the scaffold followed by a gradual remodeling process into lamellar bone alongside scaffold degradation (fig. 8). Specifically, new vessel formation is seen sprouting from the CPF axial vasculature (Fig. 4H, black arrows and J yellow arrows) with woven bone deposition surrounding vessels and scaffold struts (Fig. 4, J and O, green-colored tissue; Fig. 5B, d) and integrating with host bone from the CPF (Fig. 5B, p and d). The new bone formation is supported by endothelial ingrowth within the bone-scaffold composite (Fig. 4J, yellow arrows) with diffusely positive CD31 from H-type vessels (Fig. 5J, p to d) and diffuse vWF staining throughout the new bone regenerate (Fig. 5K, p to d). The coupling between angiogenesis and neo-osteogenesis is well reported (27), and the expression of *Notch* is key throughout this process. The presence of *Notch* supports bone regeneration and helps initiate the remodeling process. Our study demonstrated *Notch* expression at endothelial cells within the scaffold and at areas of bone remodeling (Fig. 5L, p to d) and helps link the process of new vessel formation, bone regeneration, and remodeling.

The osseoconductive PCL-TCP scaffold helps direct and support autologous precursor cells from the flap and new bone formation from the free ends of residual tibia above and below the defect. We observed a highly organized canalicular network (Fig. 4K) running perpendicular to collagen type I fibers (Fig. 4L, white arrows) and osteocytic interactions with scaffold struts that were obvious (Fig. 4K, red arrow). The aforementioned process supported the presence of ongoing bone formation with differentiating osteogenic cells (osteoblast-osteocyte like; Fig. 4J, red arrowheads) marginating the CPF host bone remnants (fig. 4J, green tissue).

Large volumes of bone regenerate with extensive mineralization were seen for the mPCL-TCP + CPF group (Fig. 3C). However, the bone appeared to be in the earlier stages of remodeling in certain parts (Fig. 4, J and O), as evidenced by poorly ordered collagen

fibers (Fig. 4J, black head arrows at green region) and a slower process of remodeling led by osteoblast-osteocyte invasion at the surface of the CPF [Fig. 5B (m), black line]. Despite this observation, in some portions of established woven bone and scaffold wall, collagen type II deposition was seen in areas of calcified cartilage (Fig. 5C, p to d), indicating that the transition to lamellar bone remodeling was well underway. This delayed remodeling was somewhat reflected in the biomechanical maturity of the M size bone defects when comparing the mPCL-TCP + CPF group with ABG (Fig. 3, A and B), where torsional stiffness was equivalent ($P = 0.46$) although torsional moment was significantly less ($P < 0.001$). Delayed remodeling of the mPCL-TCP + CPF group was considered to be related to the large portion of cortical bone tissue (naturally more resistant to remodeling than cancellous bone) placed inside the scaffold. In concert with progressive degradation of the mPCL-TCP scaffold, ongoing bone regeneration and remodeling is expected to continue in the years following the final experimental time point (16) with expected medullary cavity formation. It is recognized that the hallmark of functional bone regeneration is restoration of mechanical integrity (38). With a lack of structural integrity often seen with woven bone compared to lamellar bone, the delay in remodeling seen in the mPCL-TCP + CPF group may also help explain these biomechanical results.

Bone morphogenic activity is regulated by several antagonists including Noggin (immature cells) and Sclerostin (mature cells) (Fig. 8). At sites of high expression of collagen type II, bone formation is still desired, which may have contributed to a greater rate of mesenchymal stem cell (MSC) differentiation, and thus would explain the lack of Noggin expression. These results are further supported by Sclerostin and OPG expression at osteocytes and at osteocyte cell processes. Sclerostin, only expressed by osteocytes that have reached the osteocytic stage, is a key regulator of bone remodeling, facilitating the signaling between osteocytes, mature osteoblasts, and bone resorbing osteoclast. OPG is also important for the balance of osteoclast differentiation and activation, playing a major role in inhibiting osteoclastogenesis and bone resorption. OC is considered a late and specific osteogenic marker determining osteoblast differentiation, regulating bone crystal formation, specifically binding to hydroxyapatite crystals and down-regulating mineralization. Strong OC expression was detected in osteocytes within lacunae, at resorption pits, and in close apposition to the mPCL-TCP scaffold struts (Figs. 5D and 6N and figs. S4 and S6M). This observation confirms an emerging peak in the early phases of bone remodeling occurring at the 12-month sacrifice time point. Our results suggest that this coordinated function of Noggin, sclerostin, and OPG all together play a pivotal role in bone remodeling, osteoclastogenesis, and overall bone homeostasis (39) with OC serving as a marker of this remodeling process.

The 3D printed and patient-specific mPCL-TCP scaffold used in our case study has a robust preclinical (10, 14, 17, 18) and clinical efficacy base, with approval for use in the craniofacial region by the FDA and CE. More than 60 published clinical cases as well as more than 100,000 mPCL scaffolds being implanted globally confirm both efficacy and safety of the construct (fig. S8) (40–48). Within both the preclinical studies and the clinical case, SGBR was found radiologically and confirmed biomechanically and histologically (Fig. 4, A to O), with healthy osteocytic networks identified within the new bone and interacting with the struts of the mPCL-TCP scaffold (Fig. 4, J, K, and O) alongside new blood vessel

formation [Figs. 5, J (red color, yellow arrows) and O (red color), and 6, J and K]. Osteocytes were seen in close proximity to TCP crystals that lined the PCL struts, supporting the osseointegrative nature of the mPCL-TCP scaffold and SGBR concept (Fig. 4K). In preclinical work, scaffold degradation for the mPCL-TCP scaffold has been studied extensively (13, 49). In our study expression of CD68, a marker of macrophagic activity, was strong along the scaffold struts and at bone remodeling surfaces (Fig. 5G). M1 phenotype expression (a marker of inflammatory macrophage activity) was sparse and only seen at the endothelial tissue within blood vessels (Fig. 5H, p to d), whereas M2 anti-inflammatory phenotype expression (known to down-regulate inflammation and improve tissue repair) was strong at the mPCL-TCP-coated scaffold wall and at areas of bone remodeling (Fig. 5I, p to d), suggesting that the high mannose receptor expression was representative of a tissue remodeling/regenerative response (50, 51).

Scaffold degradation alongside bone remodeling was seen throughout the μ CT analysis at the 12-month time point for both the M and XL size preclinical groups (Figs. 4B and 6B and figs. S4B and S6B). This process was also confirmed in both SEM and PSR (Fig. 4, H to O, and fig. S5) and immunohistochemistry (IHC) results (Fig. 5), particularly in our XL size defect pilot study where the expression differential between *Notch* and *Noggin* supported a trend to remodeling when comparing 12- and 15-month animal data (Fig. 6, V to W, and fig. S6, P to Q). For in vivo work, degradation of the mPCL-TCP scaffold material occurs over 24 to 36 months (16), and in this proof-of-concept study, incomplete scaffold degradation may have contributed to incomplete secondary bone remodeling by the study end point (12 months). In our clinical case, bone samples taken from the distal site of the scaffold at the 12-month time point highlight delayed scaffold degradation despite the newly formed bone (Fig. 7, G to O). It is expected that this may be related to a relative lack of vascularity to this portion of the scaffold, which, in turn, affects macrophage-driven degradation. Furthermore, the printed porosity of the mPCL-TCP scaffold at the distal and proximal ends was less than the diaphyseal portion to facilitate more structural integrity at these sites in the construct. Nevertheless, this did not limit the patient achieving the functional outcome of full weight-bearing at the 24-month time point (movie S1).

The convergence of microvascular corticoperiosteal tissue transfer into SGBR has several advantages. Incorporating the mPCL-TCP scaffold, the RMAV concept also provides lower donor site morbidity. It is only the outer edge of the cortex that is harvested with the periosteum (movie S3), and thus, the integrity of the residual bone is largely unaltered. Donor site morbidity is a major disadvantage associated with vascularized bone transfer for large-volume segmental bone defects (5), where an entire fibula is harvested en bloc with its blood supply rather than just its very outer cortex in our case. For defects encountered like the clinical case presented, no current contemporary surgical options would suffice. The harvest of two vascularized fibula flaps poses major bone loss and would have insufficient volume to bridge the defect. Furthermore, such an approach takes from his remaining functional limb. Other options include distraction osteogenesis (4), which would have been unsuitable for this defect size because of the time and morbidity associated with acquiring that extent of distracted bone length. Despite the fact that success using the Masquelet technique has been reported for the mPCL-TCP scaffold system

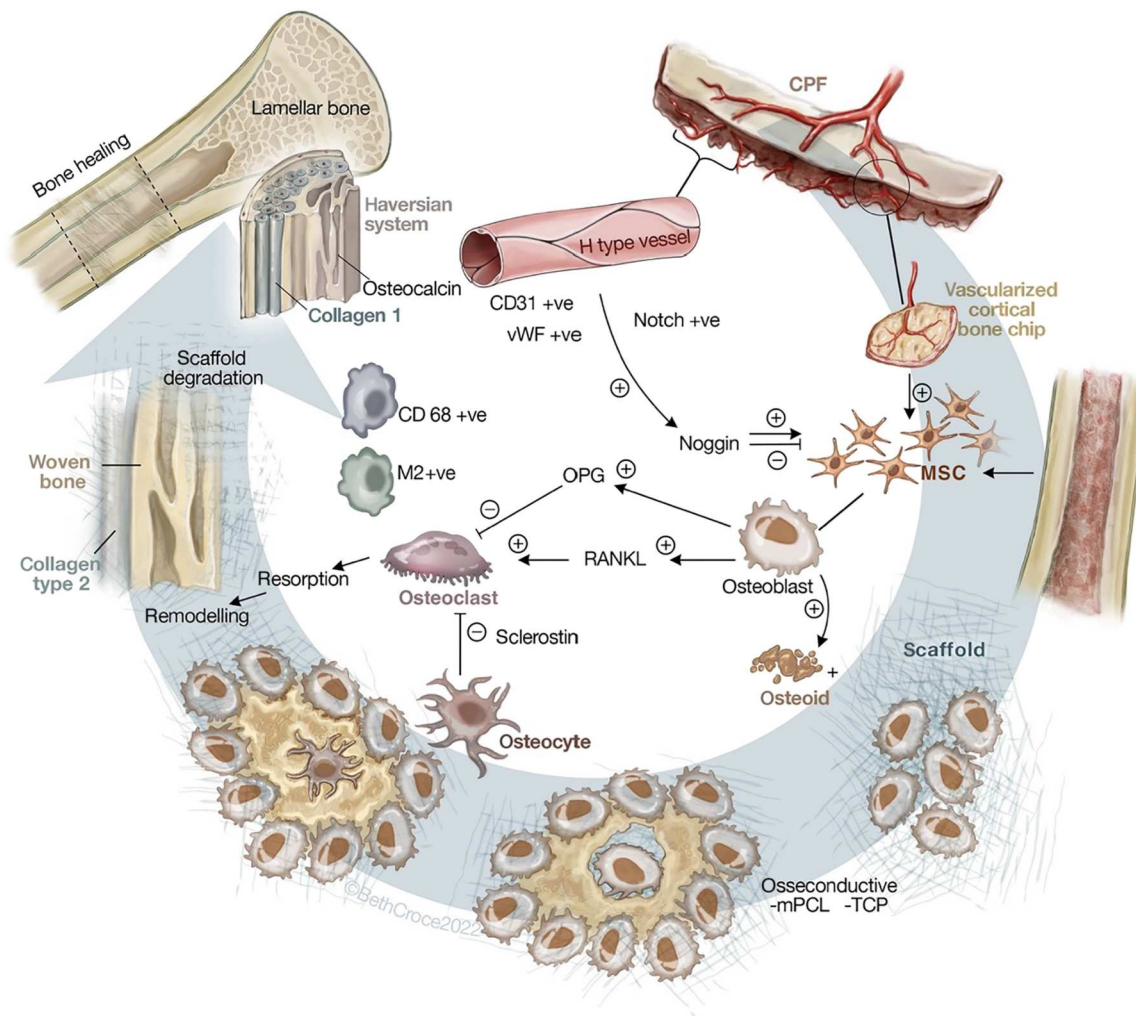


Fig. 8. Illustration demonstrating proposed sequence of events for the RMAV approach in bone regeneration based on work performed by our group (13, 15–18, 25, 40, 50) and others (51). M2, type 2 macrophages (anti-inflammatory). Credit: Beth Croce.

(46), it would be insufficient for the extent of bone loss seen in our case without a more predictable blood supply to support bone regeneration. If the Masquelet technique was performed with ABG alone, such volume of bone graft in of itself would carry considerable morbidity at a price not justifying its use, notwithstanding the lack of vasculature to ensure bone healing.

There are a number of limitations for the preclinical evaluation. Comparison of prospectively collected data between a retrospective dataset reduces the use of animals at the expense of introducing statistical bias. In sheep from mPCL-TCP only and ABG groups, the defect was stabilized with a 10-hole DCP compared with a 12-hole DCP in the mPCL-TCP + CPF group. We attempted to control for this difference in the prospective study by placing screws further away from the defect, thereby lengthening the working force of the plate to ensure biomechanical equivalence between the groups. We used vascularized corticoperiosteal tissue transfer with additive rhBMP-7, as we had independent validation from extensive preclinical work that, individually, these modalities enhanced bone regeneration with the mPCL-TCP scaffold (17, 25). Amalgamation of the two techniques in the clinical arena was

considered to be the optimal approach for bone regeneration, with the lack of bone regeneration in humans using rhBMP-7 serving to support the larger role of the CPF in our positive study results. Vascularity of the flap at the terminal study end point was not validated in vivo using direct measures (microspheres, etc.), although bone formation, its pattern of regeneration, and the presence of new blood vessel formation emanating from the CPF serve as indirect measures (Fig. 4J). In the in vivo study, the mPCL-TCP + CPF group is compared against a scaffold control group (mPCL-TCP) and the clinical gold standard for small segment bone defects (ABG). No comparison was made to a CPF-only control group, as this was a proof-of-principle study, and the clinical application of this method was intended for extensive bone defects where a scaffold would inherently be required to guide the bone regenerative process. A recent clinical trial by Morrison and co-workers (52) using a tissue engineering chamber to create larger volumes of adipose tissue further supports this concept. Only one of five patients developed sufficient adipose tissue for breast reconstructive purposes (210 ml), and the authors attribute this to the lack of scaffold guidance among

other limitations. Reviewing our own pilot study results, incorporation of the mPCL-TCP scaffold with the CPF showed substantial bone regeneration (Figs. 4 and 5 and figs. S4 and S6), supporting the concept of SGBR (20).

Over a 7-year period (fig. S9), the work presented highlights the successful transition from a preclinical proof-of-principle study to a clinical case (Fig. 7). For the patient, there were very limited reconstructive options for the affected limb, and therefore, this approach was offered, as a limb-salvage procedure, given its perceived efficacy in humans at the time. To our knowledge, our case represents the most extensive load-bearing bone reconstruction in the literature using a SGBR approach, and it is the first to incorporate the RMAV approach. The second largest comparable size long bone reconstruction using a 3D printed scaffold was described by Horch *et al.* (8 cm in length and 2.5 cm diameter) with a scaffold (36), also performed for osteomyelitis. In their report, they used an arteriovenous loop model to vascularize the scaffold intrinsically axially and reported satisfactory bone healing at 2-year follow up. Other studies with less extensive long bone defects have been successful using a scaffold-guided approach (46, 53, 54), which validates the SGBR concept in bone regeneration (20). Clinical follow up for our case study was 48 months, and last imaging at 36 months after surgery supported success of the RMAV reconstruction (movie S2). Given the success of our approach to bone regeneration, a phase IIa clinical trial in Brisbane at a major trauma center is registered and approaching the enrolment phase (ANZCTR no. 12620001007921).

This study introduces an original approach for SGBR with clinical translation in the most extensive bone reconstruction performed to date with the use of a 3D printed scaffold. This opens new avenues to the reconstructive surgical community with an interest in regenerative medicine to take the marriage between tissue engineering and modern surgical practice to new heights.

MATERIALS AND METHODS

In vivo study

Study design

The objective of this research was to confirm the efficacy of an integrative approach to M size critical bone reconstruction in a validated preclinical model and to show that this approach can be safely extended to a larger XL defect size. The in vivo work is reported in line with the Animal Research: Reporting of In Vivo Experiments guidelines (55), and relevant Institutional Animal Care and Use Committee guidelines were followed for animal subjects. Specifically, ethics approval was obtained from the Queensland University of Technology (QUT) University Animal Ethics Committee (approval numbers: 1600000280, 700000915, and 900000906). The in vivo component of this paper was performed using our well-established M size segmental bone defect sheep model (10, 14, 17–19). A total of 10 healthy castrated male merino sheep (*Ovis aries*, 6 to 8 years of age, body weight of 45 to 65 kg) were procured for the study through the QUT Medical Engineering Research Facility (MERF) at Prince Charles Hospital (Chermside, Queensland, Australia), without genetic modification or previous medical/surgical procedures. Sheep were chosen as the animal model for this study because of the research unit experience and also the extensive use of this model in bone tissue engineering due to notable crossover in bone morphology and physiology to humans (56, 57). As

realistically as possible, large animal models also provide a means to reproduce the relevant loading conditions and surgical technique as used in the final procedure in humans (56, 57).

The first phase of the study involved three groups of sheep ($n = 23$) with M size segmental defects of the tibial diaphysis. Experimental groups included defects treated with either (i) an mPCL-TCP scaffold alone ($n = 7$), (ii) mPCL-TCP scaffold with a CPF ($n = 8$), or (iii) ABG ($n = 8$). Data involving animals from the groups with mPCL-TCP alone and ABG were collected from a retrospective dataset using the same large animal protocol (17), in line with the three “R” concept of ethical animal research (replacement, reduction, and refinement). We chose a comparable number for our mPCL-TCP + CPF study group in line with previous work (17), and no randomization or blinding was performed as part of this in vivo study. The study period was a 12-month time interval during which all animals were able to weight-bear immediately following the operation in a sling for 2 weeks. Following this, animals were freed to mobilize. The delayed end point of 12 months was decided upon to enable the evaluation of the long-term effects of vascularized corticoperiosteum on bone regeneration and remodeling, as well as the evaluation of the mPCL-TCP scaffold material, and to compare against existing retrospective datasets for mPCL-TCP alone (scaffold control) and ABG (clinical gold standard control). Progressive x-ray was performed on the sheep during the study period at the following intervals: 6 weeks, 3 months, 6 months, 9 months, and 12 months. Radiographic (x-ray and μ CT), biomechanical, histological, immunohistochemical, polarized light microscopy (LPM), and SEM analyses of the hindlimbs were then performed following animal sacrifice.

Outcome measures for analysis in the M size study included objective measures of bone healing such as torsional stiffness and torsional moment, as well as bone volume regenerate characteristics of the defect as measured with μ CT. Plain radiography, histological, and immunohistochemistry analyses were performed in a descriptive fashion for this study.

Pilot study

The second phase of the study involved a pilot evaluation the mPCL-TCP scaffold and CPF ($n = 2$) in the same animal model using a larger XL defect size (6 cm in length). Only two sheep were used for this component of the study, as it was sufficient to confirm feasibility of the approach and was consistent with pilot study sample size requirements by our institution (QUT). This was performed to determine the role of this method in regenerating bone for a more clinically relevant defect size as an antecedent to clinical translation. Sheep bone regeneration was analyzed in an identical fashion to the M size defect study (x-ray, biomechanics, μ CT, histology, SEM, and IHC), although no comparison to an alternative treatment group could be performed. One sheep was evaluated for a total study time length of 15 months and the other for 12 months, to compare bone remodeling at a later time point.

Scaffold preparation

The mPCL-TCP scaffold was additively manufactured as described previously (17). Briefly, for the M size defect, the cylindrical and centrally fenestrated mPCL-TCP scaffolds were manufactured using an outer diameter of 20 mm, an inner diameter of 8 mm, and a height of 30 mm (Osteopore International Pty Ltd., Singapore). For the XL size defect, the height of the scaffold was raised to 60 mm. For both M and XL size studies, the scaffold was halved into two pieces to facilitate placement of the CPF and tied back

together using a 3/0 Vicryl tie (Ethicon, Bridgewater, USA). The scaffold was placed into the defect en bloc for the mPCL-TCP-only group. Scaffold characteristics included a porosity of 70% with fully interconnected pores of dimension determined by the filament diameter (300 μm) and separation (1200 μm) with a 0/90° lay down pattern.

Operative approach

After induction of anesthesia, the sheep was placed in right-sided recumbency, the left hind leg was tied, and the medial right hind leg was exposed for surgery. The sheep's right tibia was exposed and preplated with a DCP to delineate the defect and definitive fixation in advance. In the mPCL-TCP CPF group, the cranial tibial vascular pedicle was identified and dissected free from the tibial nerve before raising the CPF, effectively periosteal tissue from the tibial defect with a thin layer of cortical bone with its blood supply intact (fig. S10, A to D, and movie S3). A longitudinal length of 3 cm was harvested with a 4-cm standardized circumferential width of resection from the anterior surface of the tibia (fig. S10, A to D). For two sheep, this was increased to a longitudinal length of 6 cm in the large-defect pilot study, with the same circumferential width of resection (4 cm). Next for all groups, using an oscillating saw and a saw guide, proximal and distal osteotomies were performed to excise 3 cm of tibia in the mid-diaphysis (fig. S10C). The defect was increased to an XL size (6 cm length) in the pilot study. Care was taken to completely remove the periosteum in the defect area 1 cm proximal and distal to the defect and from the muscular septum and to not damage the neurovascular bundle. The CPF was then inserted inside the endosteal surface of the mPCL-TCP scaffold with the pedicle entering from a custom segment excision in the proximal end of the cortical bone (fig. S10E). Before plating, flap perfusion was confirmed visually by observation of visible pulsatility of the flap pedicle in the distal scaffold.

The DCP and screws were reinserted to stabilize the M size defect site, which was filled with an mPCL-TCP + CPF (fig. S10F). In the XL size pilot study, the defect was also filled with an mPCL-TCP + CPF. After mPCL-TCP scaffold implantation and defect stabilization, the muscular fascia and panniculus carnosus were repaired using 3/0 Vicryl (Ethicon, Bridgewater, USA) in a layered manner to achieve full soft tissue coverage of the tibial bone and the defect site. Following this, the skin was closed using the same suture material. After completion of the surgical procedure, x-ray images in two planes (anteroposterior and true lateral) were taken to ensure correct implant placement and exclude any bony pathology.

A soft-ban synthetic cast (BSN Medical, Mount Waverly, Australia) was placed over the leg for 6 weeks postoperatively. During the first postoperative week, the animals were kept in a load-sharing harness to limit weight bearing on the limb. Next, the animals were permitted to weight bear and mobilize in a controlled manner within a penned area. They were gradually transferred to a larger outside penned area at MERF for up to 12 weeks postoperatively for free mobilization before transfer back to the farm until the study period had concluded (12 months after surgery).

Plain radiography

Medial-lateral and anterior-posterior views using plain radiography (3.2 mA·s and 65 kV) were performed to progressively assess the extent of bone regeneration across the defect following surgery ($t = 0$ days) at 1, 3, 6, 9, and 12 months to determine radiographic features of regenerate bone formation and bony union. The time to defect bridging was also recorded.

Biomechanical testing

After animal sacrifice, the operated tibiae were disarticulated from the hindlimb and assessed as described previously (17, 18). Briefly, both tibial ends were embedded in 80 ml of deformable Paladur (Kulzer; Emgrid, catalog no. 64707938) and mounted into a biaxial testing machine (Instron 8874). Torsion under angular displacement at a targeted velocity of 0.5/s and constant compression load of 0.05 kN was performed until the first signs of fracture were observed. The contralateral tibia was used as a paired reference. Values for torsional stiffness and torsional moment were calculated and normalized against the values of the contralateral tibiae.

Micro-computed tomography

A $\mu\text{CT}40$ (M size, mPCL-TCP and ABG groups) or $\mu\text{CT}50$ (M and XL, mPCL-TCP + CPF groups) μCT (Scanco Medical AG) was used to image and quantify the newly formed mineralized tissue after animal sacrifice. Specimens were placed in a tube filled with ethanol and scanned at a voltage of 70 kilovolt peak (kVp), a current of 114 mA, and an isotropic voxel size of 18 and 17.2 μm for $\mu\text{CT}40$ and $\mu\text{CT}50$, respectively. The analyzed volume of interest included the defect region only. Acquired images were segmented with a Gaussian filter of a width of 0.8 and support of 1.0. Thresholds were determined by visual evaluation of 20 random tomograms/specimen of four samples per group and then kept constant for all samples. The bone volume (BV; mm^3) of defects was analyzed for total volume (BV_{total}), and this was subdivided into three equal divisions axially (proximal, middle, and distal) and radially (inside scaffold, scaffold wall, and outside scaffold) for further characterization of bone regeneration as described previously (17, 19).

Histology and IHC analysis

Histology and immunohistochemistry were performed according to Sparks *et al.* (18). The antibodies used for this study are detailed in table S2.

Scanning electron microscopy

For visualization of the osteocyte network in the mPCL-TCP + CPF group, resin sections were ground at 100 μm and acid-etched with 37% phosphoric acid (Ajax Finechem, Albany, NZ, catalog no. AJA371-2.5LPL) for 3 s and in 12.5% sodium hypochlorite (Ajax Finechem, Albany, NZ, catalog no. AJA82-500G) for 5 min. Resin sections were then gold-sputtered at 30 mA for 95 s (Leica EM SCD005, Leica Microsystems, New South Wales, Australia). A TESCAN MIRA 3 (Tescan, Brno, Czech Republic) high-resolution electron microscope was used to image the resin sections using an accelerating voltage of 5.0 kV and beam intensity of 8.0 at a constant 8-mm working distance.

Statistical analysis

Statistical analysis was carried out using GraphPad Prism version 7.03 (GraphPad Software, La Jolla, CA, USA) for the *in vivo* study. Comparison was made between mPCL-TCP only, mPCL-TCP + CPF, and ABG groups. Outcome measures assessed included μCT evaluation (bone volume total, bone volume axial, and bone volume radial) and biomechanical characteristics (maximal torsional stiffness and polar moment of inertia, i.e., torsional moment) of the healed bone. The Mann-Whitney *U* and one-way analysis of variance (ANOVA) tests were used to compare individual treatment groups where necessary. Significance was defined as $P < 0.05$.

Clinical case Study design

In conjunction with our interdisciplinary team, the objective of this part of the study was to confirm the results of the pre-clinical large animal study in a challenging clinical case where no alternative reconstructive option was available to the patient. The clinical case was reviewed for suitability to undergo an experimental procedure by the Metro South Health Clinical Ethics Committee (31.3.2017). Regulatory approval for use of the mPCL-TCP scaffold (Osteopore International Pty Ltd., Singapore) was granted through the Special Access Scheme of the Therapeutic Goods Administration Australia. The patient provided informed consent for the experimental procedure.

3D bone reconstruction and scaffold design

Once tissue culture test results of specimens taken from the proximal and distal residual tibia were reported clear, this rendered the defect unmistakably defined. The patient's lower extremities were reimaged with CT angiography (Siemens SOMATOM Definition Flash, Erlangen, Germany) using iodinated contrast medium (350 mg/ml; Optiray 350, Liebel-Flarsheim Company, Oceanside, CA, USA). The voxel size was set at 0.826 mm by 0.826 mm by 0.5 mm. The stack of 2D grayscale CT images was processed using Amira (version 6.2.0, FEI-Thermo Fisher Scientific, Oregon, USA). The tibia and fibula of both legs were segmented by applying a global threshold to create 3D models of the affected and the intact contralateral tibiae. The 3D models were converted into STL file format and imported into Netfabb (Autodesk Inc., San Rafael, CA, USA) for design of the 3D printed scaffold. The intact contralateral tibia model was mirrored, rotated, and remodeled to align anatomically with the defect, which served as a template for the scaffold design. Proximal and distal endosteal extensions of the scaffold were incorporated into the design to reduce the risk of implant dislocation. The scaffold model was then split into posterior (2/3 circumference) and anterior (1/3 circumference) components and hollowed to accommodate the intramedullary nail and CPFs. After the final geometry and fit of the scaffold model were confirmed through prototype 3D printing of the defect site and the scaffold, the 3D model of the scaffold was rendered porous. The porosity of the body of the scaffold was set at 80% to facilitate vascularization and cell attachment. The porosity of the endosteal extensions was set at 40% to neutralize forces tending to dislocate the implant at its interface with host bone. Implant stability was enhanced by defining a specific fiber lay down pattern (0°/60°/120°) during the 3D-printing process. The final scaffold design for implantation was then 3D-printed in an mPCL-TCP by Osteopore (Osteopore International Pty Ltd., Singapore; fig. S8). The 3D printed scaffold was gamma-sterilized and shipped.

Supplementary Materials

This PDF file includes:

Tables S1 and S2

Figs. S1 to S13

Legends for movies S1 to S3

Other Supplementary Material for this manuscript includes the following:

Movies S1 to S3

REFERENCES AND NOTES

1. D. S. Sparks, M. Wagels, G. I. Taylor, Bone reconstruction: A history of vascularized bone transfer. *Microsurgery* **38**, 7–13 (2018).
2. J. K. Chan, L. Harry, G. Williams, J. Nanchahal, Soft-tissue reconstruction of open fractures of the lower limb: Muscle versus fasciocutaneous flaps. *Plast. Reconstr. Surg.* **130**, 284e–295e (2012).
3. A. C. Masquelet, T. Begue, The concept of induced membrane for reconstruction of long bone defects. *Orthop. Clin. North Am.* **41**, 27–37 (2010).
4. G. A. Ilizarov, V. I. Ledyasev, V. P. Shitin, The course of compact bone reparative regeneration in distraction osteosynthesis under different conditions of bone fragment fixation (experimental study). *Eksp. Khir. Anesteziol.* **14**, 3–12 (1969).
5. D. S. Sparks, D. B. Saleh, W. M. Rozen, D. W. Hutmacher, M. A. Schuetz, M. Wagels, Vascularised bone transfer: History, blood supply and contemporary problems. *J. Plast. Reconstr. Aesthet. Surg.* **70**, 1–11 (2017).
6. A. Misaghi, T. J. Jackson, A. A. Stans, W. J. Shaughnessy, P. S. Rose, S. L. Moran, M. T. Houdek, Intercalary allograft reconstruction of the proximal tibia with and without a free fibula flap in pediatric patients. *J. Pediatr. Orthop.* **40**, e833–e838 (2020).
7. K. M. Klifto, S. C. Azoury, C. S. Klifto, S. Mehta, L. S. Levin, S. J. Kovach, Treatment of post-traumatic tibial diaphyseal bone defects: A systematic review and meta-analysis. *J. Orthop. Trauma* **36**, 55–64 (2022).
8. M. J. Bosse, E. J. MacKenzie, J. F. Kellam, A. R. Burgess, L. X. Webb, M. F. Swionkowski, R. W. Sanders, A. L. Jones, M. P. McAndrew, B. M. Patterson, M. L. McCarthy, T. G. Trivison, R. C. Castillo, An analysis of outcomes of reconstruction or amputation after leg-threatening injuries. *N. Engl. J. Med.* **347**, 1924–1931 (2002).
9. J. Henkel, M. A. Woodruff, D. R. Epari, R. Steck, V. Glatt, I. C. Dickinson, P. F. M. Choong, M. A. Schuetz, D. W. Hutmacher, Bone regeneration based on tissue engineering conceptions - A 21st century perspective. *Bone Res.* **1**, 216–248 (2013).
10. A. Berner, J. D. Boerckel, S. Saifzadeh, R. Steck, J. Ren, C. Vaquette, J. Q. Zhang, M. Nerlich, R. E. Guldberg, D. W. Hutmacher, M. A. Woodruff, Biomimetic tubular nanofiber mesh and platelet rich plasma-mediated delivery of BMP-7 for large bone defect regeneration. *Cell Tissue Res.* **347**, 603–612 (2012).
11. A. Berner, J. Henkel, M. A. Woodruff, S. Saifzadeh, G. Kirby, S. Zaiss, J. Gohlke, J. C. Reichert, M. Nerlich, M. A. Schuetz, D. W. Hutmacher, Scaffold-cell bone engineering in a validated preclinical animal model: Precursors vs differentiated cell source. *J. Tissue Eng. Regen. Med.* **11**, 2081–2089 (2017).
12. A. Berner, J. C. Reichert, M. A. Woodruff, S. Saifzadeh, A. J. Morris, D. R. Epari, M. Nerlich, M. A. Schuetz, D. W. Hutmacher, Autologous vs. allogenic mesenchymal progenitor cells for the reconstruction of critical sized segmental tibial bone defects in aged sheep. *Acta Biomater.* **9**, 7874–7884 (2013).
13. A. Cipitria, C. Lange, H. Schell, W. Wagermaier, J. C. Reichert, D. W. Hutmacher, P. Fratzl, G. N. Duda, Porous scaffold architecture guides tissue formation. *J. Bone Miner. Res.* **27**, 1275–1288 (2012).
14. A. Cipitria, J. C. Reichert, D. R. Epari, S. Saifzadeh, A. Berner, H. Schell, M. Mehta, M. A. Schuetz, G. N. Duda, D. W. Hutmacher, Polycaprolactone scaffold and reduced rhBMP-7 dose for the regeneration of critical-sized defects in sheep tibiae. *Biomaterials* **34**, 9960–9968 (2013).
15. A. Cipitria, W. Wagermaier, P. Zaslansky, H. Schell, J. C. Reichert, P. Fratzl, D. W. Hutmacher, G. N. Duda, BMP delivery complements the guiding effect of scaffold architecture without altering bone microstructure in critical-sized long bone defects: A multiscale analysis. *Acta Biomater.* **23**, 282–294 (2015).
16. C. X. Lam, D. W. Hutmacher, J. T. Schantz, M. A. Woodruff, S. H. Teoh, Evaluation of polycaprolactone scaffold degradation for 6 months in vitro and in vivo. *J. Biomed. Mater. Res. A* **90**, 906–919 (2009).
17. J. C. Reichert, A. Cipitria, D. R. Epari, S. Saifzadeh, P. Krishnakanth, A. Berner, M. A. Woodruff, H. Schell, M. Mehta, M. A. Schuetz, G. N. Duda, D. W. Hutmacher, A tissue engineering solution for segmental defect regeneration in load-bearing long bones. *Sci. Transl. Med.* **4**, 141ra193 (2012).
18. D. S. Sparks, S. Saifzadeh, F. M. Savi, C. E. Dlasaka, A. Berner, J. Henkel, J. C. Reichert, M. Wulschleger, J. Ren, A. Cipitria, J. A. McGovern, R. Steck, M. Wagels, M. A. Woodruff,

- M. A. Schuetz, D. W. Hutmacher, A preclinical large-animal model for the assessment of critical-size load-bearing bone defect reconstruction. *Nat. Protoc.* **15**, 877–924 (2020).
19. J. Henkel, F. Medeiros Savi, A. Berner, S. Fountain, S. Saifzadeh, R. Steck, D. R. Epari, M. A. Woodruff, M. Knackstedt, M. A. Schuetz, D. W. Hutmacher, Scaffold-guided bone regeneration in large volume tibial segmental defects. *Bone* **153**, 116163 (2021).
 20. D. S. Sparks, F. M. Savi, S. Saifzadeh, M. A. Schuetz, M. Wagels, D. W. Hutmacher, Convergence of scaffold-guided bone reconstruction and surgical vascularization strategies—A quest for regenerative matching axial vascularization. *Front. Bioeng. Biotechnol.* **7**, 448 (2019).
 21. A. Das, E. Botchwey, Evaluation of angiogenesis and osteogenesis. *Tissue Eng. Part B Rev.* **17**, 403–414 (2011).
 22. R. Hertel, A. Gerber, U. Schlegel, J. Cordey, P. Rügsegger, B. A. Rahn, Cancellous bone graft for skeletal reconstruction. Muscular versus periosteal bed—preliminary report. *Injury* **25**Suppl 1, A59–A70 (1994).
 23. D. B. Jones Jr., H. Burger, A. T. Bishop, A. Y. Shin, Treatment of scaphoid waist nonunions with an avascular proximal pole and carpal collapse. A comparison of two vascularized bone grafts. *J. Bone Joint Surg. Am.* **90**, 2616–2625 (2008).
 24. N. Leibig, J. O. Wietbrock, A. K. Bigdeli, R. E. Horsch, T. Kremer, U. Kneser, V. J. Schmidt, Flow-induced axial vascularization: The arteriovenous loop in angiogenesis and tissue engineering. *Plast. Reconstr. Surg.* **138**, 825–835 (2016).
 25. D. S. Sparks, F. Medeiros Savi, S. Saifzadeh, M. L. Wille, M. Wagels, D. W. Hutmacher, Bone regeneration exploiting corticoperiosteal tissue transfer in scaffold-guided bone regeneration. *Tissue Eng. Part C Methods* **28**, 202–213 (2022).
 26. Y. Peng, S. Wu, Y. Li, J. L. Crane, Type H blood vessels in bone modeling and remodeling. *Theranostics* **10**, 426–436 (2020).
 27. S. K. Ramasamy, A. P. Kusumbe, L. Wang, R. H. Adams, Endothelial Notch activity promotes angiogenesis and osteogenesis in bone. *Nature* **507**, 376–380 (2014).
 28. Food and Drug Administration (FDA), *Guidance Document for Industry and CDRH Staff for the Preparation of Investigational Device Exemptions and Premarket Approval Applications for Bone Growth Stimulator Devices* (63 FR 23292, April 28, 1998).
 29. J. P. M. Frölke, P. Patka, Definition and classification of fracture non-unions. *Injury* **38**, S19–S22 (2007).
 30. J. M. Kanczler, R. O. Oreffo, Osteogenesis and angiogenesis: The potential for engineering bone. *Eur. Cell. Mater.* **15**, 100–114 (2008).
 31. A. M. Parfitt, The mechanism of coupling: A role for the vasculature. *Bone* **26**, 319–323 (2000).
 32. C. K. Colton, Implantable biohybrid artificial organs. *Cell Transplant.* **4**, 415–436 (1995).
 33. P. H. Warnke, I. N. G. Springer, J. Wiltfang, Y. Acil, H. Eufinger, M. Wehmöller, P. A. J. Russo, H. Bolte, E. Sherry, E. Behrens, H. Terheyden, Growth and transplantation of a custom vascularised bone graft in a man. *The Lancet* **364**, 766–770 (2004).
 34. O. O. Erol, M. Spira, New capillary bed formation with a surgically constructed arteriovenous fistula. *Plast. Reconstr. Surg.* **66**, 109–115 (1980).
 35. O. C. Cassell, W. A. Morrison, A. Messina, A. J. Penington, E. W. Thompson, G. W. Stevens, J. M. Perera, H. K. Kleinman, J. V. Hurley, R. Romeo, K. R. Knight, The influence of extracellular matrix on the generation of vascularized, engineered, transplantable tissue. *Ann. N. Y. Acad. Sci.* **944**, 429–442 (2001).
 36. R. E. Horsch, J. P. Beier, U. Kneser, A. Arkudas, Successful human long-term application of in situ bone tissue engineering. *J. Cell. Mol. Med.* **18**, 1478–1485 (2014).
 37. D. W. Buck II, G. A. Dumanian, Bone biology and physiology: Part I. The fundamentals. *Plast Reconstr. Surg.* **129**, 1314–1320 (2012).
 38. J. C. Reichert, thesis, Queensland University of Technology, Kelvin Grove, Australia (2010).
 39. A. G. Robling, L. F. Bonewald, The osteocyte: New insights. *Annu. Rev. Physiol.* **82**, 485–506 (2020).
 40. D. W. Hutmacher, J. T. Schantz, C. X. Lam, K. C. Tan, T. C. Lim, State of the art and future directions of scaffold-based bone engineering from a biomaterials perspective. *J. Tissue Eng. Regen. Med.* **1**, 245–260 (2007).
 41. J.-T. Schantz, T.-C. Lim, C. Ning, S. H. Teoh, K. C. Tan, S. C. Wang, D. W. Hutmacher, Cranioplasty after trephination using a novel biodegradable burr hole cover: Technical case report. *Neurosurgery* **58** (Suppl. 1), ONS-E176 (2006).
 42. S. W. Low, Y. J. Ng, T. T. Yeo, N. Chou, Use of osteoplug polycaprolactone implants as novel burr-hole covers. *Singapore Med. J.* **50**, 777–780 (2009).
 43. S. Seen, S. Young, S. S. Lang, T. C. Lim, S. Amrith, G. Sundar, Orbital implants in orbital fracture reconstruction: A ten-year series. *Craniofacial. Trauma Reconstr.* **14**, 56–63 (2021).
 44. S. Seen, S. M. Young, S. J. Teo, S. S. Lang, S. Amrith, T. C. Lim, G. Sundar, Permanent versus bioresorbable implants in orbital floor blowout fractures. *Ophthalmic. Plast. Reconstr. Surg.* **34**, 536–543 (2018).
 45. Y. Ming, N. H. J. Hui, D. W. N. Vincent, N. Chou, Y. T. Tsai, Cranial reconstruction using a polycaprolactone implant after burr hole trephination. *J. 3D Print. Med.* **4**, 9–16 (2020).
 46. P. Kobbe, M. Laubach, D. W. Hutmacher, H. Abdulrahman, R. M. Sellei, F. Hildebrand, Convergence of scaffold-guided bone regeneration and RIA bone grafting for the treatment of a critical-sized bone defect of the femoral shaft. *Eur. J. Med. Res.* **25**, 70 (2020).
 47. M. E. Cheng, J. Janzekovic, H. J. Theile, C. Rutherford-Heard, M.-L. Wille, C. Cole, T. B. Lloyd, R. J. W. Theile, M. Wagels, D. W. Hutmacher, Pectus excavatum camouflage: A new technique using a tissue engineered scaffold. *Eur. J. Plast. Surg.* **45**, 177–182 (2021).
 48. G. Castrosos, I. G. Matheus, D. Sparks, M. Lowe, N. Ward, M. Sehu, M. L. Wille, Y. Phua, F. M. Savi, D. Hutmacher, M. Wagels, Regenerative matching axial vascularisation of absorbable 3D-printed scaffold for large bone defects: A first in human series. *J. Plast. Reconstr. Aesthet. Surg.* **75**, 2108–2118 (2022).
 49. J. C. Reichert, M. E. Wulschleger, A. Cipitria, J. Lienau, T. K. Cheng, M. A. Schütz, G. N. Duda, U. Nöth, J. Eulert, D. W. Hutmacher, Custom-made composite scaffolds for segmental defect repair in long bones. *Int. Orthop.* **35**, 1229–1236 (2011).
 50. C. A. Lahr, F. Wagner, A. Shafiee, M. Rudert, D. W. Hutmacher, B. M. Holzapfel, Recombinant human bone morphogenetic protein 7 exerts osteo-catabolic effects on bone grafts that outweigh its osteo-anabolic capacity. *Calcif. Tissue Int.* **105**, 331–340 (2019).
 51. Z. Chen, C. Wu, W. Gu, T. Klein, R. Crawford, Y. Xiao, Osteogenic differentiation of bone marrow MSCs by β -tricalcium phosphate stimulating macrophages via BMP2 signalling pathway. *Biomaterials* **35**, 1507–1518 (2014).
 52. W. A. Morrison, D. Marre, D. Grinsell, A. Batty, N. Trost, A. J. O'Connor, Creation of a large adipose tissue construct in humans using a tissue-engineering chamber: A step forward in the clinical application of soft tissue engineering. *EBioMedicine* **6**, 238–245 (2016).
 53. M. Marcacci, E. Kon, V. Moukhachev, A. Lavroukov, S. Kutepov, R. Quarto, M. Mastrogiacomo, R. Cancedda, Stem cells associated with macroporous bioceramics for long bone repair: 6- to 7-year outcome of a pilot clinical study. *Tissue Eng.* **13**, 947–955 (2007).
 54. P. Šponer, T. Kučera, J. Brtková, K. Urban, Z. Kočí, P. Měříka, A. Bezrouk, Š. Konrádová, A. Filipová, S. Filip, Comparative study on the application of mesenchymal stromal cells combined with tricalcium phosphate scaffold into femoral bone defects. *Cell Transplant.* **27**, 1459–1468 (2018).
 55. N. P. du Sert, V. Hurst, A. Ahluwalia, S. Alam, M. T. Avey, M. Baker, W. J. Browne, A. Clark, I. C. Cuthill, U. Dirnagl, M. Emerson, P. Garner, S. T. Holgate, D. W. Howells, N. A. Karp, S. E. Lazic, K. Lidster, C. J. MacCallum, M. Macleod, E. J. Pearl, O. H. Petersen, F. Rawle, P. Reynolds, K. Rooney, E. S. Sena, S. D. Silberberg, T. Steckler, H. Würbel, The ARRIVE guidelines 2.0: Updated guidelines for reporting animal research. *PLOS Biol.* **18**, e3000410 (2020).
 56. J. A. McGovern, M. Griffin, D. W. Hutmacher, Animal models for bone tissue engineering and modelling disease. *Dis. Model. Mech.* **11**, dmm033084 (2018).
 57. J. C. Reichert, D. R. Epari, M. E. Wulschleger, S. Saifzadeh, R. Steck, J. Lienau, S. Sommerville, I. C. Dickinson, M. A. Schütz, G. N. Duda, D. W. Hutmacher, Establishment of a preclinical ovine model for tibial segmental bone defect repair by applying bone tissue engineering strategies. *Tissue Eng. Part B Rev.* **16**, 93–104 (2010).

Acknowledgments: We thank A. Gibbon, C. Bartlett, K. Logan, and other staff at the QUT Medical Engineering Research Facility for veterinary assistance and administrative and technical support. We thank D. Blomberger and R. Steck for assistance with biomechanical testing. We thank S. Eggert and N. J. Castro for assistance in the prototype printing. We thank the hospital staff involved in the clinical case for clinical involvement, and we would like to thank J. Richardson for administrative support. The type II collagen (II-6B3) antibody was purchased from the Developmental Studies Hybridoma Bank, created by the NIH and maintained at the University of Iowa, Department of Biology (USA). **Funding:** The in vivo study was funded through grants awarded through the Australian Research Council; Princess Alexandra Hospital Research Foundation; Wesley Research Foundation, Brisbane; and the Berlin-Brandenburg Center for Regenerative Therapies. The scaffold used in the clinical case was provided without cost by Osteopore (Osteopore, International Pty Ltd., Singapore). **Author contributions:** D.S.S. was responsible for experimental design; developing the animal model; performing all animal surgeries, x-rays, mechanical testing, specimen preparation, and μ CT scans; and assisting with histological analysis and was primarily responsible for drafting the paper. F.M.S. was responsible for biomechanical analysis, specimen preparation, histological analysis, and SEM and assisted with manuscript preparation. S.S. was responsible for developing the animal model and performing all animal surgeries and x-rays. C.E.D. was responsible for developing the animal model and performing all animal surgeries. G.B. was responsible for μ CT scans and associated analysis and assisted with manuscript preparation. E.R. was responsible for specimen preparation and histological analysis and assisted with manuscript editing. A.C. and J.C.R. were responsible for previously collected data, which included performing animal surgeries, x-rays, μ CT scans and analyses, and histological analyses, and participated in manuscript editing. M.-L.W. was responsible for scaffold design, prototype 3D printing, and preparation for the clinical case and contributed to manuscript preparation and assisted in the μ CT scanning and performed μ CT data analysis. N.W. was involved in the operative management of the clinical case and contributed to manuscript preparation. M.W. was primarily responsible for designing

and performing the operative approach in the clinical case. M.A.S. was involved in in vivo study design/supervision and contributed to manuscript preparation. D.W.H. and M.W. initiated and directed the project, conceived and facilitated design the experiments, oversaw the collection of results and data interpretation, and finalized the paper. D.S.S., M.W., and D.W.H. conceived the idea of the RMAV strategy. **Competing interests:** D.W.H. is a shareholder in Osteopore (Osteopore International Pty Ltd., Singapore). The remaining authors declare that they have no

competing interests. **Data and materials availability:** All data needed to evaluate the conclusions in the paper are present in the paper and/or the Supplementary Materials.

Submitted 22 June 2022

Accepted 4 April 2023

Published 5 May 2023

10.1126/sciadv.add6071

Convergence of scaffold-guided bone regeneration principles and microvascular tissue transfer surgery

David S. Sparks, Flavia M. Savi, Constantin E. Dlaska, Siamak Saifzadeh, Gary Brierly, Edward Ren, Amaia Cipitria, Johannes C. Reichert, Marie-Luise Wille, Michael A. Schuetz, Nicola Ward, Michael Wagels, and Dietmar W. Hutmacher

Sci. Adv., **9** (18), eadd6071.
DOI: 10.1126/sciadv.add6071

View the article online

<https://www.science.org/doi/10.1126/sciadv.add6071>

Permissions

<https://www.science.org/help/reprints-and-permissions>

Use of this article is subject to the [Terms of service](#)

Science Advances (ISSN) is published by the American Association for the Advancement of Science. 1200 New York Avenue NW, Washington, DC 20005. The title *Science Advances* is a registered trademark of AAAS.

Copyright © 2023 The Authors, some rights reserved; exclusive licensee American Association for the Advancement of Science. No claim to original U.S. Government Works. Distributed under a Creative Commons Attribution NonCommercial License 4.0 (CC BY-NC).